



저작자표시-비영리-변경금지 2.0 대한민국

이용자는 아래의 조건을 따르는 경우에 한하여 자유롭게

- 이 저작물을 복제, 배포, 전송, 전시, 공연 및 방송할 수 있습니다.

다음과 같은 조건을 따라야 합니다:



저작자표시. 귀하는 원저작자를 표시하여야 합니다.



비영리. 귀하는 이 저작물을 영리 목적으로 이용할 수 없습니다.



변경금지. 귀하는 이 저작물을 개작, 변형 또는 가공할 수 없습니다.

- 귀하는, 이 저작물의 재이용이나 배포의 경우, 이 저작물에 적용된 이용허락조건을 명확하게 나타내어야 합니다.
- 저작권자로부터 별도의 허가를 받으면 이러한 조건들은 적용되지 않습니다.

저작권법에 따른 이용자의 권리는 위의 내용에 의하여 영향을 받지 않습니다.

이것은 [이용허락규약\(Legal Code\)](#)을 이해하기 쉽게 요약한 것입니다.

[Disclaimer](#)

공학석사 학위논문

**Porous N, S co-doped Carbon Materials
from Natural Resources as Counter
Electrode for Dye-Sensitized Solar Cells**

천연 물질로 합성한 질소 및 황이 도핑된
다공성 탄소 물질의 염료감응태양전지
상대전극으로의 적용

2017년 2월

서울대학교 대학원

화학생물공학부 에너지환경화학융합기술전공

손윤준

**Porous N, S co-doped Carbon Materials
from Natural Resources as Counter
Electrode for Dye-Sensitized Solar Cells**

지도교수 성 영 은




이 논문을 공학석사학위논문으로 제출함

2017년 2월

서울대학교 대학원
화학생물공학부
에너지환경화학기술융합전공
손 윤 준

손윤준의 석사학위논문을 인준함

2017년 2월

위원장	<u>한 태 환</u>	
부위원장	<u>성 영 은</u>	
위원	<u>김 대 형</u>	

Abstract

Porous N, S co-doped Carbon Materials from Natural Resources as Counter Electrode for Dye-Sensitized Solar Cells

Yoon Jun Son

Chemical Convergence for Energy & Environment

School of Chemical & Biological Engineering

The Graduate School

Seoul National University

In the face of global energy and environmental crisis, renewable energy sources have become crucial as alternatives to fossil fuels. Among many energy sources, dye-sensitized solar cells (DSSCs) are attractive for their simple fabrication, low cost, and high power conversion efficiency. However, expensive Pt electrocatalyst, which has been conventionally used for triiodide reduction, should be substituted for more inexpensive alternative catalysts for large scale fabrication of DSSCs. Alternative catalysts are

required to be highly electrocatalytically active and conductive as well as inexpensive and Earth-abundant.

Many researchers have investigated alternative electrocatalysts, such as Pt-based alloys, transition metal alloys, transition metal compounds, conducting polymer and carbonaceous materials. Among these alternatives, carbonaceous materials have merits of lower cost and abundance. Whereas, intrinsic electrocatalytic activity of carbonaceous materials for triiodide reduction reaction is quite low. To overcome the low intrinsic activity of carbonaceous materials, various approaches like increasing roughness by tuning morphologies of the electrodes or increasing active sites by doping heteroatoms into carbonaceous materials have been tried. However, these approaches require expensive instruments or harsh and complex experimental conditions.

In this research, we introduced waste coffee-grounds as a green electrocatalyst, especially for the triiodide reduction reaction. The coffee-grounds served as heteroatom-containing carbon precursors and were transformed into highly porous N,S co-doped carbon catalysts by one-step carbonization and activation process using ZnCl_2 salt. The counter electrodes (CEs) were fabricated by spraying the obtained coffee catalyst ink onto the FTO glass. The activated coffee (AC) electrode exhibited superior

electrocatalytic activity compared to non-activated coffee (NC) electrode due to tenfold increase in roughness of the electrode without significant loss of intrinsic catalytic activity. Also, the AC-CE exhibited better electrocatalytic activity than Pt-CE with charge transfer resistance (R_{ct}) values at the interface of CE/electrolyte being $0.46 \Omega \text{ cm}^2$ and $1.46 \Omega \text{ cm}^2$ for AC-CE and Pt-CE. DSSC with AC-CE showed higher photovoltaic performance with a fill factor (FF , 73.2 %), a short circuit current density (J_{sc} , 15.07 mA/cm^2), and a power conversion efficiency (η , 8.37 %), while those of the DSSC with Pt-CE were 71.0 %, 14.93 mA/cm^2 , and 8.06 %, respectively. In this research, carbon CE made from cheap and abundant coffee-grounds was proved to be a successful alternative to the Pt-CE.

Keywords: dye-sensitized solar cells (DSSCs), counter electrode (CE), triiodide reduction reaction, coffee-grounds, ZnCl_2 activation.

Student Number: 2015-21024

성명 : 손 윤 준

Contents

Abstract	i
Contents	iv
List of Tables	vi
List of Figures	vii
Chapter 1. Introduction	1
1.1. General Introduction to Dye-Sensitized Solar Cells	1
1.2. Structure and Principle of DSSCs	2
1.3. Components	4
1.3.1. Sensitizer	4
1.3.2. Working electrode	7
1.3.3. Redox electrolyte	8
1.3.4. Counter electrode	13
1.4. Solar Cell Performance Measurement	15
1.5. Objective of this Dissertation	19
Chapter 2. Experimental	24
2.1. Preparation of coffee counter electrodes	24
2.2. Preparation of the Pt counter electrode and working electrode	25

2.3. Preparation of the iodide redox electrolytes	26
2.4. Fabrication of symmetric dummy cells and solar cells	26
2.5. Material characterization, electrochemical analyses, and photovoltaic performance evaluation	27
Chapter 3. Results and Discussion	30
3.1. Material synthesis and characterization	30
3.2. Electrocatalytic activity and stability of the coffee electrodes	47
3.3. Application of the coffee electrodes in dye-sensitized solar cells	61
Chapter 4. Conclusions	65
Reference	67
국문초록 (Korean Abstract)	75

List of Tables

Table 3.1. Nitrogen sorption data of the NC and AC catalysts.	36
Table 3.2. Composition of NC and AC samples obtained from (a) EA, and (b) XPS.	39
Table 3.3. Content distributions of N states in NC and AC catalysts.	42
Table 3.4. Summary of electrical resistivity (ρ) and conductivity (σ) from a four-point probe and series resistance (R_s) from EIS of symmetrical cells. ..	46
Table 3.5. Parameters obtained from cyclic voltammogram for the I_3^-/I^- redox reaction.	49
Table 3.6. Electrochemical parameters determined by fitting the impedance spectra of symmetrical dummy cells with Pt, NC, and AC electrodes.	57
Table 3.7. Kinetic parameters for triiodide reduction reaction and obtained apparent activation energies on different counter electrodes.	60
Table 3.8. Summary of J - V characteristic for DSSCs using different counter electrodes under 1 sun illumination (AM 1.5 G, 100 mW cm ⁻²).	63

List of Figures

- Figure 1.1.** (a) Schematic of conventional configuration of the dye-sensitized solar cells, including TiO₂ photoanode on TCO, dye molecules, liquid electrolyte and counter-electrode. (b) Schematic of operation of the dye-sensitized solar cells.3
- Figure 1.2.** Molecular structure of (a) ruthenium-based dyes: N3, N719, N749 (b) organic dye: Y123 (c) porphyrin dyes: SM373, SM315.6
- Figure 1.3.** Photocurrent-voltage curve of a DSSC using I⁻/I₃ redox electrolyte at different light intensities.10
- Figure 1.4.** (a) Gerischer diagram of the dye-sensitized solar cell with iodide/ triiodide electrolyte. The level of the unstable reaction intermediate (I₂⁻) is indicated. (b) Schematic of energy level of redox couple for dye-sensitized solar cell.11
- Figure 1.5.** Molecular structure of (a) tris bipyridine cobalt complex, (b) bis bipyridine-pyrazole cobalt complex, and (c) TEMPO/TEMPO⁺. (d) Energy diagram for dye-sensitized solar cells using various redox couples with different energy levels.12
- Figure 1.6.** (a) Power conversion efficiency of DSSCs using various

transition metal compounds CE. (b) Illustration of calculated E_a^{dis} of I_2 , E_a^{des} of I^* and corresponding activity as a function of E_{ad}^1 . (c),(d) Adsorption energy of I atom on different CE materials and on different adsorption sites determined by DFT calculation.16

Figure 1.7. Photon flux and accumulated photocurrent of the AM 1.5 G spectrum at 1000W m^{-2}18

Figure 3.1. (a) Photographs showing the fabrication process of counter electrode using coffee catalysts. (b) Schematic of a dye-sensitized solar cell with coffee catalyst as counter electrode.31

Figure 3.2. TEM image of coffee-grounds powder (a, b) after carbonization at $800\text{ }^\circ\text{C}$ in Ar and (c, d) after carbonization and activation with ZnCl_2 simultaneously at $800\text{ }^\circ\text{C}$ in Ar.33

Figure 3.3. Top-view SEM images of coffee catalysts sprayed onto the FTO glass. (a, b) non-activated coffee catalyst, (c, d) activated coffee catalyst.34

Figure 3.4. (a) Nitrogen adsorption and desorption isotherms. (b) Pore size distribution of coffee catalysts.35

Figure 3.5. XRD patterns of NC and AC catalysts.38

Figure 3.6. (a) High resolution N1s XPS spectra of coffee-grounds powder with and without ZnCl_2 activation. Deconvoluted nitrogen peaks:

pyridinic-N (398.5 eV), pyrrolic-N (400.3 eV), graphitic-N (401 eV).

(b) Content distributions of nitrogen states in NC and AC.41

Figure 3.7. EF-TEM images of AC. (a) TEM image and the corresponding elemental mapping of (b) carbon, (c) nitrogen, (d) sulfur.43

Figure 3.8. (a) Comparison of Raman spectra of NC and AC in the wavenumber range 1000 – 1900 cm^{-1} . (b) Comparison of D/G ratio in NC and AC.45

Figure 3.9. (a) Cyclic voltammograms obtained at a scan rate of 50 mV/s for oxidation and reduction of the I_3^-/I^- redox couple using different electrocatalysts as the WE, a Pt mesh as the CE, Ag/AgNO₃ as the reference electrode from -0.6 V to 1.0 V. (b) Cathodic peak potential of Pt, NC, and AC in I_3^-/I^- electrolytes.48

Figure 3.10. Cyclic voltammograms of (a) Pt, (b) NC, (c) AC CE for I_3^-/I^- redox couples at different scan rates (from inner to outer: 10, 25, 50, 75, 100 mV s^{-1}). (d) Relationship between cathodic peak current density and square root of scan rates.51

Figure 3.11. Cyclic voltammograms of 100 cycles using (a) Pt, (b)NC, (c) AC as working electrodes at a scan rate of 50 mV s^{-1} ,(d) cathodic current density as a function of number of CV cycle.52

Figure 3.12. (a) Tafel polarization curves of symmetric dummy cells

with Pt, NC, and AC counter electrodes for iodide electrolytes. (b) Impedance spectra of the symmetric dummy cells for iodide electrolytes, with the insets showing the enlarged spectra. Both analyses were conducted at 20 °C.54

Figure 3.13. The equivalent circuit model for the impedance spectra of symmetric dummy cells shown in Figure 3.12b.55

Figure 3.14. (a) Nyquist plots of symmetric dummy cell of NC electrode at five different temperature conditions. (b) Arrhenius plot of the temperature dependence of the charge transfer resistance (left ordinate) and exchange current density (right ordinate) to determine the apparent activation energy for triiodide reduction reaction with different counter electrodes.59

Figure 3.15. (a) Photocurrent density-voltage (J-V) curves of DSSCs with different counter electrodes under 1 sun illumination (AM 1.5 G, 100mW cm⁻²). (b) IPCE spectra of the DSSCs with different counter electrodes.63

Chapter 1. Introduction

1.1. General introduction to dye-sensitized solar cells

Nowadays, world energy consumption keeps increasing as world's population grows rapidly over 7 billion. This has caused the excessive usage of fossil fuels which are limited resources. Also, greenhouse gases and other toxic substances emitted from fossil fuels bring about serious world-wide social issues, such as global warming and environmental pollution. To cope with global energy and environmental crisis, it has become crucial to develop environmental-friendly sustainable energy sources, such as wind, biomass, hydropower and solar energy. Among these energy sources, solar energy has great potential to resolve global energy crisis since the Earth receives 170,000 terawatts of incoming solar radiation per year which is sufficient to fully meet the energy demand of the mankind [1].

There are several kinds of methods to convert solar energy into useful form of energy, such as hydrogen, various organic materials, or electricity. Since electricity is the most useful and efficient form of energy, solar cells that can convert solar energy into electricity drew a lot of attention. Until now, silicon-based solar cells are universal due to their high efficiency and stability. However, the fabrication process of silicon-based solar cells has serious demerits of high costs and energy consumption.

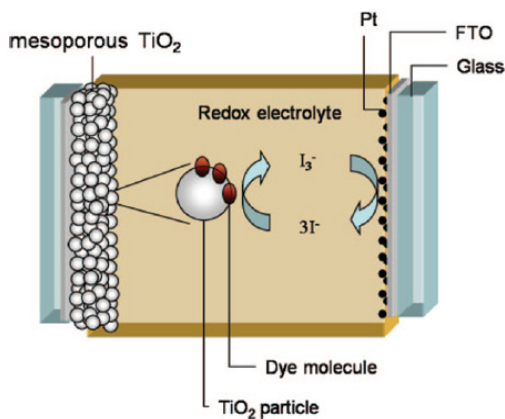
Due to these serious shortcomings of silicon-based solar cells, scientists researched various kinds of solar cells as alternatives to conventional silicon-based solar cells, such as inorganic compound solar cells, organic solar cells, polymer solar cells, hybrid solar cells, etc. Amongst them is the dye-sensitized solar cell (DSSC) that mimics the photosynthesis mechanism of plants. Dye-sensitized solar cells (DSSC) have attracted Dye-sensitized solar cell was first reported by O'Regan and Michael Grätzel in 1991 [2], and gained remarkable importance because of their low production costs, simple fabrication process and high light-to-electricity conversion efficiency.

1.2. Structure and principle of DSSCs

Conventional dye-sensitized solar cells consist of three major components: working electrode, redox electrolyte, and counter electrode. The working electrode is comprised of transparent conductive oxide (TCO), semiconductor electrode and sensitizer. Thin layer of dye sensitizer is adsorbed on the semiconductor electrode deposited on the transparent conductive oxide (TCO). Figure 1.1a shows the components and structure of DSSC.

Dye-sensitized solar cell (DSSC) is operated mainly through six steps. First, the dye molecules adsorbed on the semiconductor film absorb incident light, generating excited photoelectrons and being oxidized. Second, excited photoelectrons are rapidly injected into the conduction band of semi-

(a)



(b)

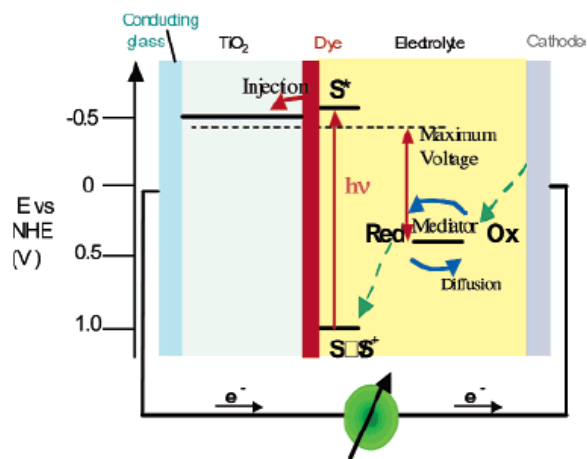


Figure 1.1. (a) Schematic of conventional configuration of the dye-sensitized solar cells, including TiO₂ photoanode on TCO, dye molecules, liquid electrolyte and counter-electrode. (b) Schematic of operation of the dye-sensitized solar cells. (Adapted from Hagfeldt, A. et al., *Chem. Rev.* **2010**, *110*, 6595-6663. and Grätzel, M., *Inorg. Chem.* **2005**, *44*, 6841-6851.)

conductor film. Third, injected electrons are transported through the semiconductor film to the transparent conductive oxide (TCO) glass by diffusion due to the gradient in electron concentration. Fourth, transparent conductive oxide collects electrons and electrons flow to the counter electrode through external circuit. Through this fourth step, useful form of energy, electricity, is obtained. Fifth, after dye molecules become oxidized, dye molecules are regenerated by redox couple in electrolyte and redox couple is oxidized. Sixth, oxidized redox couple moves to the counter electrode and gets reduced by combining with electrons from external circuit. Considering the redox couple in DSSCs is regenerative type, through the above operation cycle as shown in Figure 1.1b, DSSCs can operate continuously without net chemical changes.

1.3. Components

1.3.1. Sensitizer

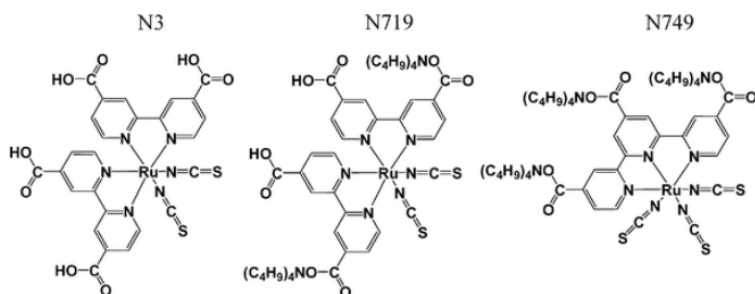
The mechanism of dye-sensitized solar cell (DSSC) is very similar to the photosynthesis in nature and sensitizer plays a most fundamental role in DSSC like chlorophyll in the photosynthesis. Sensitizers are adsorbed on the semiconductor surface by chemical bonds and play a role to harvest solar light and generate photoelectrons by exciting electrons in HOMO (Highest

Occupied Molecular Orbital) to LUMO (Lowest Unoccupied Molecular Orbital).

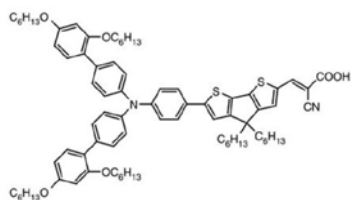
There are various types of sensitizers, such as metal complexes [3-6], porphyrin dyes [7-10], organic dyes [11-13], etc. Among these, ruthenium-based dyes, such as N3, N719 and N749 dye, are generally used with iodide/triiodide (I^-/I_3^-) redox mediator and porphyrin or organic dyes, such as Y123, YD2-o-C8, are used with cobalt-based redox mediators. Figure 1.2 shows molecular structure of representative dyes.

There are five conditions for ideal sensitizer in DSSCs. First, sensitizer dye should have more positive ground-state potential than redox potential and negative excited-state potential than that of conduction band edge of semiconductor oxide for regenerative photoelectrochemical cells. Second, dye should have broad absorption spectrum [1]. Third, dyes with high extinction coefficient are required. Even high performance dyes waste quite a lot of solar energy even in the wavelength range below their absorption threshold wavelength. Fourth, long excited-state lifetime and chemical stability are demanded for practical applications. Because in order to provide practical photovoltaics, it is mandatory that solar cells maintain performance for 50-100 million turnovers corresponding to about 20 years operation [14]. Fifth, electron injection from the excited dye to the semiconductor oxide

(a)



(b)



(c)

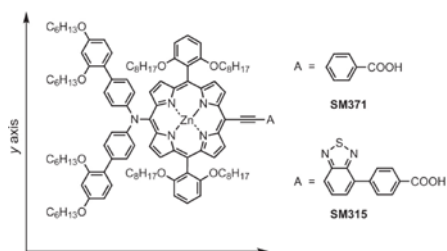


Figure 1.2. Molecular structure of (a) ruthenium-based dyes: N3, N719, N749 (b) organic dye: Y123 (c) porphyrin dyes: SM373, SM315. (Adapted from Lee, Y. et al., *New J Chem.* **2007**, *31*, 2120-2126 and Yum, J. et al., *Nat. Commun.* **2012**, *3*, 631 and Mathew, S. et al., *Nat. Chem.* **2014**, *6*, 242-247)

should be so fast as to reduce loss of electrons by thermal relaxation of the molecular excited state and increase injection efficiency [15].

1.3.2. Working electrode (WE)

Working electrode is comprised of transparent conductive oxide (TCO), semiconductor electrode, and dye sensitizer. Semiconductor electrode is deposited on the TCO glass and covered with thin layer of dye. Fluorine doped tin oxide (FTO) or indium tin oxide (ITO) are generally used as TCO and deposited on glass. TCO glass is transparent for light transmission and conductive for charge collection.

The role of semiconductor electrode is to provide sites for dye adsorption and transport electrons injected from dye to current collector. Desirable semiconductor electrode is required to have large surface area for dye loading so as to harvest light effectively and transport photoelectrons from dye to external circuit rapidly with minimal loss.

Semiconductor materials, such as TiO_2 [16-17], ZnO [18-21], and SnO_2 [22], have been investigated as the working electrode for DSSCs. Among these candidate materials, TiO_2 exhibits better solar cell performances than other semiconductor materials. In addition, other superior properties of TiO_2 , such as suitable energy level of conduction and valence band edge, chemical

stability, non-toxicity and low price, caused TiO₂ to be widely used as semiconductor electrode for DSSCs.

Various kinds of morphology and structure such as nanoparticles, nanorods, nanofibers, nanotubes, and other hierarchical structures also have been investigated for efficient working electrode. Among these, a 10 μm thick film composed of mesoporous anatase TiO₂ nanoparticles with diameters of 18 ~ 20 nm has been generally used in order to provide large surface area in spite of the demerits, such as recombination and slow electron transport induced by grain boundaries between nanoparticles [1].

1.3.3. Redox electrolyte

The key role of redox electrolyte in DSSCs is to reduce the oxidized sensitizers. After regenerating sensitizers, redox electrolyte moves to the counter electrode and gets reduced, commensurating the electrochemical circuit. Due to the role of redox electrolyte, net chemical change of the system does not happen. There are largely three categories of redox electrolytes in DSSC: liquid electrolyte [23], quasi-solid electrolyte [24], and solid-state hole conductors [25]. Among these, liquid electrolytes are most widely used because of its high performance.

Redox electrolytes have great effect on cell efficiency. There are several conditions for effective redox shuttles, such as fast dye regeneration,

slow recombination near the photoanode and faster electron transfer kinetics at counter electrode. Moreover, how close energy level of the redox couple is to the D^+/D energy level is critical since the photo-voltage of a DSSC is determined by the difference between the quasi-Fermi level of electrons in the semiconductor oxide electrode and Nernst potential of the redox electrolyte.

Most widely used electrolytes are triiodide/iodide based electrolytes, because these electrolytes show not only desirable kinetic properties like fast dye regeneration and slow recombination at photoanode, but also high stability. In 2005, M. Grätzel reported that cell efficiency reached 11.4% using I^-/I_3^- redox couples as shown in Figure 1.3. However, triiodide/iodide redox couple have its limitation in that this absorbs blue light, decreasing photocurrent and I_3^- corrodes current collector like Ag and Cu when scaling up. In addition, high driving force (about 0.6V) is required for dye regeneration due to two electron transfer process (Figure 1.4a), causing V_{oc} loss (Figure 1.4b). Recently, as alternatives to iodide/triiodide redox couples, transition metal complex like cobalt based polypyridyl (Figure 1.5a), organic redox shuttle, such as TEMPO (Figure 1.5b), T^-/T_2 thiolate, with more positive redox potential also have been researched vigorously [26-30] as shown in Figure 1.5c.

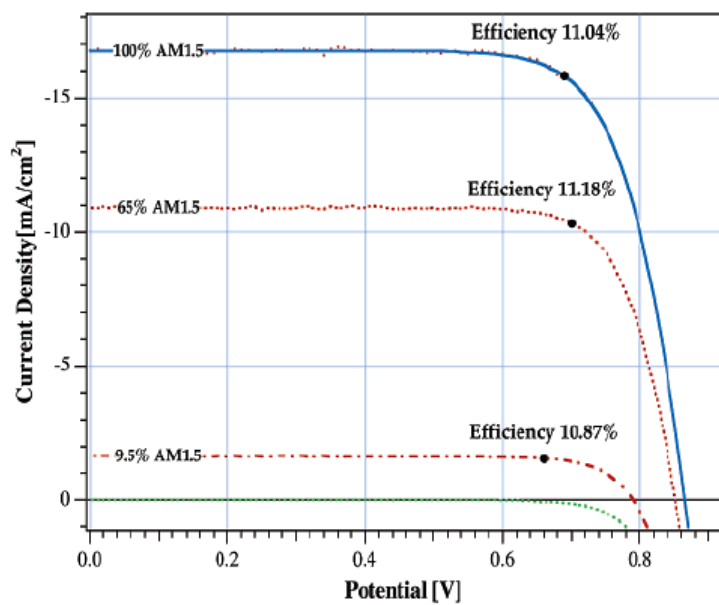
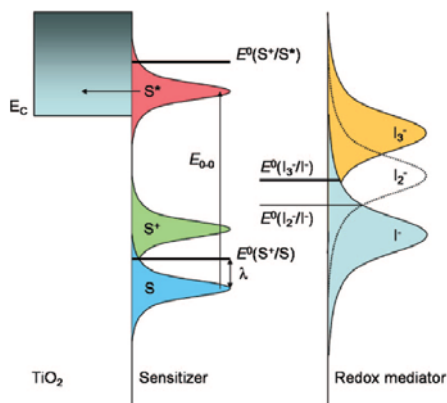


Figure 1.3. Photocurrent-voltage curve of a DSSC using I/I_3 redox electrolyte at different light intensities. (Adapted from Grätzel, M., *Inorg. Chem.* **2005**, *44*, 6841-6851)

(a)



(b)

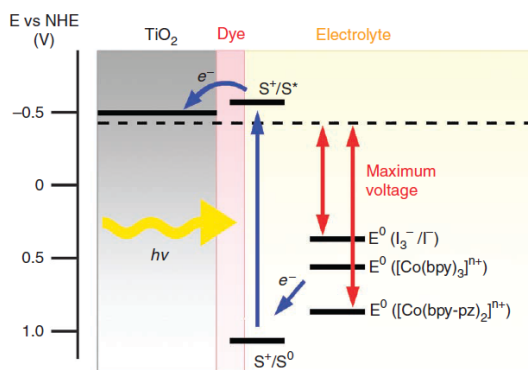


Figure 1.4. (a) Gerischer diagram of the dye-sensitized solar cell with iodide/ triiodide electrolyte. The level of the unstable reaction intermediate (I_2^-) is indicated. (b) Schematic of energy level of redox couple for dye-sensitized solar cell. (Adapted from Hagfeldt, A. et al., *Chem. Rev.* **2010**, *110*, 6595-6663 and Yum, J. et al., *Nat. Commun.* **2012**, *3*, 631)

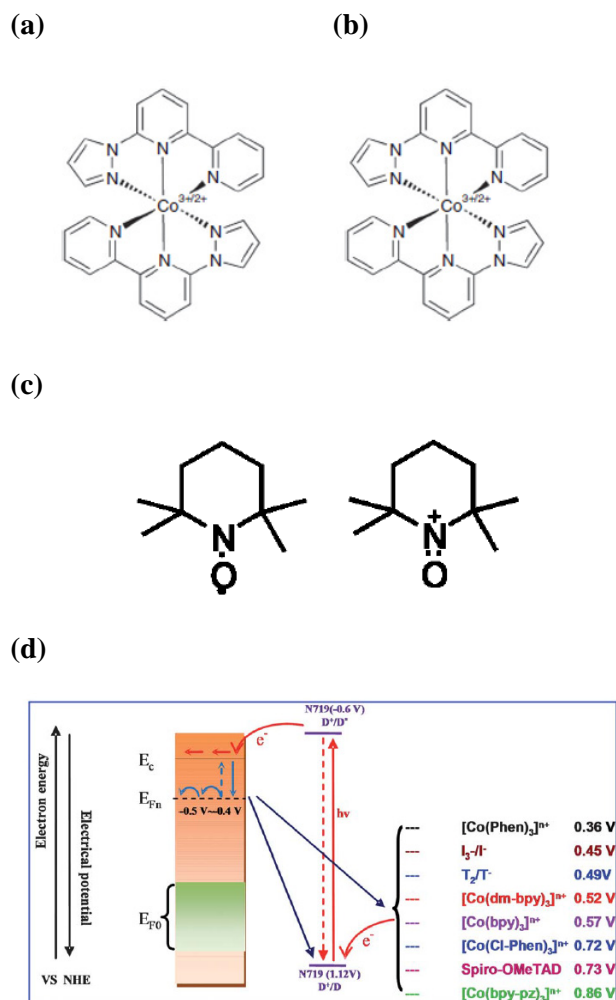


Figure 1.5. Molecular structure of (a) tris bipyridine cobalt complex, (b) bis bipyridine-pyrazole cobalt complex, and (c) TEMPO/TEMPO⁺. (d) Energy diagram for dye-sensitized solar cells using various redox couples with different energy levels. (Adapted from Yum, J. et al., *Nat. Commun.* **2012**, *3*, 631 and Wang, M. et al., *Energy Environ. Sci.* **2012**, *5*, 9394)

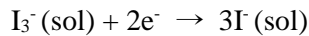
1.3.4. Counter electrode (CE)

The counter electrode (CE) is one of the most important components in DSSCs. Counter electrode usually consists of TCO glass and catalysts deposited on the TCO glass. The task of the CE is to collect electrons from outer circuit or holes from the hole transporting materials and transfer electrons to reduce the oxidized form of redox couples. However, kinetics of redox reaction on the bare FTO glass is quite slow, showing high charge transfer resistance (R_{ct}). Therefore, a desirable counter electrode should possess high conductivity and excellent catalytic activity toward redox reaction and for lowering kinetic overpotential. Also, chemical stability in electrolyte, simple fabrication, and low production costs are recommended. Platinum (Pt) coated on FTO is generally used as a counter electrode in DSSCs due to its high catalytic activity for reduction of triiodide, high conductivity. However, Pt has fatal flaws such as high cost, scarcity in nature and instability due to decomposition to PtI_4 in I^-/I_3^- electrolyte [31-32].

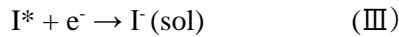
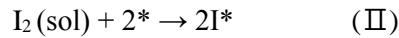
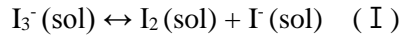
Thus, there have been efforts to reduce Pt-content in CE by alloying Pt with transition metals like Ni, Co, Fe, and so on [33-35]. Above this, carbonaceous materials [32], conducting polymers [36-43], metal alloys [44] and transition metal compounds (like sulfides, nitrides, carbides, selenides, and oxides, etc.) [45-52] have attracted great attention as cost-effective Pt-free counter electrodes with high activity and stability. Figure 1.6a shows previous

reports on performance of various kinds of Pt-free counter electrodes.

Recently, researchers have investigated on rational design of highly active catalysts for various kinds of electrochemical reactions including iodide reduction reaction (IRR). Triiodide reduction reaction (IRR) on the CE can be written as:



Above reaction can be divided into three elementary steps as follows:



, where sol exhibits the acetonitrile solution and * means the free site on the CE surface. Since the reaction step (I) is the solution reaction and usually very fast enough to be in equilibrium, reaction step (II) and (III) on the liquid-solid interface which are dissociative adsorption of I₂ and desorption of I* respectively are rate determining steps for triiodide reduction reaction. The adsorption energy of I atom (E_{ad}^I) at electrolyte/electrode interface is defined as below equation [53].

$$E_{\text{ad}}^{\text{I}} = E (\text{interface}) + 1/2E (\text{I}_2) - E (\text{I}/\text{interface})$$

Considering that adsorption energy of I atom is related to the activation barrier of reaction step (II) and (III) by Brønsted-Evans-Polanyi (BEP)

relationship, this can be used as an activity descriptor [53].

Figure 1.6b shows volcano shaped activity curve on IRR, meaning optimum adsorption energy exists for high performance catalyst. Adsorption energy can be controlled by materials, composition, facets, adsorption sites and so on, and adsorption energy for good CE ranges from 0.33 to 1.20 eV as shown in Figure 1.6c-1.6d.

1.4. Solar cell performance measurement

For the measurement of solar cell efficiency, the standard solar spectrum of AM 1.5 G is generally used as shown in Figure 1.3 [1]. ‘AM’ and ‘G’ stand for air mass and global, respectively. Air mass 1.5 means that effective thickness of Earth’s atmosphere through which radiation passes is 1.5 times longer than Earth’s atmosphere thickness and solar zenith angle is 48.2 °. Global means it considers both direct and diffuse sunlight while ‘D’ only considers direct sunlight at specific angle. The amount of radiant energy per unit area, 1000 W/m², is used as standard. The solar to electrical energy conversion efficiency (η) is defined as

$$\eta = \frac{J_{sc} V_{oc} FF}{P_{in}} \quad (1.1)$$

where J_{sc} is photocurrent density measured at short-circuit, V_{oc} is the open-circuit photovoltage which is the difference between fermi level of

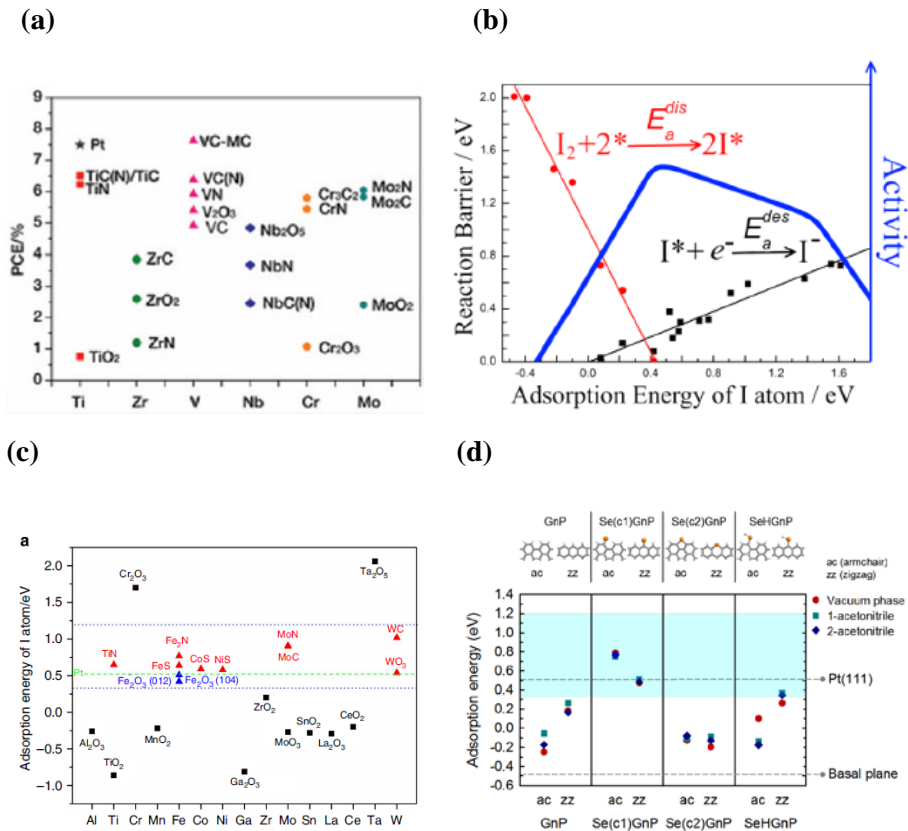


Figure 1.6. (a) Power conversion efficiency of DSSCs using various transition metal compounds CE (b) Illustration of calculated E_a^{dis} of I_2 , E_a^{des} of I^* and corresponding activity as a function of E_{ad}^I . (c),(d) Adsorption energy of I atom on different CE materials and on different adsorption sites determined by DFT calculation. (Adapted from Wu, M. et al. *J. Am. Chem. Soc.* **2012**, *134*, 3419–3428, Wang, D. et al., *ACS Catal.* **2016**, *6*, 733–741, Hou, Y. et al., *Nat. Commun.* **2013**, *4*,1583, and Ju, M, J. et al., *Sci. Adv.* **2016**, *2*, 6.)

semiconductor oxide and redox potential , FF is the fill factor of the cell, and P_{in} the intensity of the incident light. The fill factor (FF) has value between 0 and 1 and is defined as

$$FF = \frac{P_{max}}{J_{sc} V_{oc}} \quad (1.2)$$

,where P_{max} is the product of the photocurrent and photovoltage where power output is maximum. Incident photon to current conversion efficiency (IPCE) is another essential measurement of the performance of solar cell. IPCE measurement contains information about the monochromatic quantum efficiency of a solar cell. Therefore, IPCE is measured as a function of wavelength and defined as

$$IPCE = \frac{J_{sc}(\lambda)}{e \Phi(\lambda)} = 1240 \frac{J_{sc}(\lambda) [A\ cm^{-2}]}{\lambda [nm] P_{in}(\lambda) [W\ cm^{-2}]} \quad (1.3)$$

,where e is the elementary charge and λ is the wavelength of monochromatic illumination.

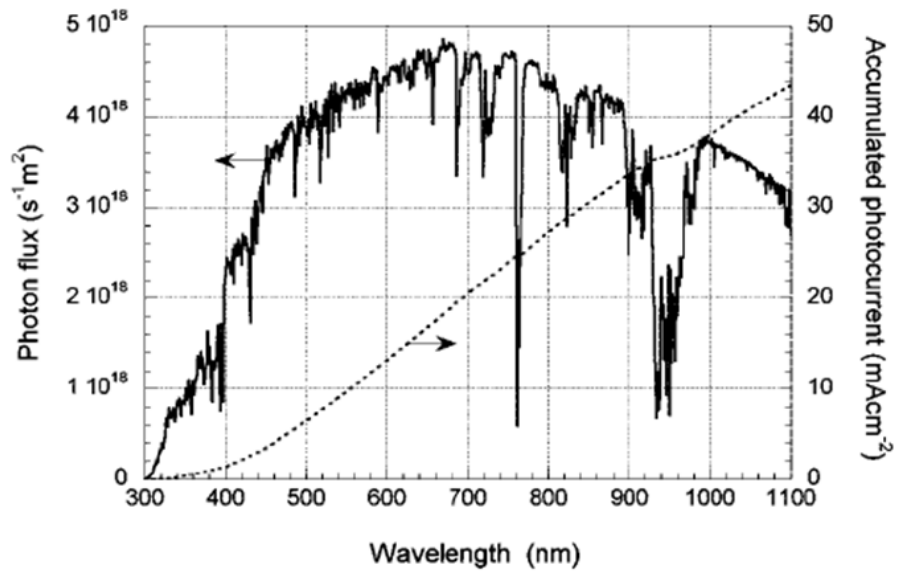


Figure 1.7. Photon flux and accumulated photocurrent of the AM 1.5 G spectrum at 1000W m^{-2} .(Adapted from Hagfeldt, A. et al., *Chem. Rev.* **2010**, *110*, 6595-6663)

1.5. Objective of this dissertation

Since first invented in 1991 by O'Regan and Grätzel [2], dye-sensitized solar cells (DSSCs) have received a lot of attention due to their simple fabrication and low production cost compared with silicon based photovoltaics. Also, DSSCs are differentiated from other photovoltaics in that DSSCs segregate light harvesting part and charge separation part, giving more options for material selection. Moreover, DSSCs use environment-friendly materials while thin film solar cells use hazardous compounds including heavy metals.

Among four key components of DSSC: photoanode, dye, electrolyte, and counter electrode, counter electrode (CE) plays a important role to collect electrons from external circuit and catalyze the reduction of I_3^- to I^- . The role of CE is very critical for solar cell performance, since counter electrode can affect the regeneration rate of oxidized form of dye, thereby changing the fill factor (FF) and photocurrent [54].

Usually, due to its high performance, platinum (Pt)-based catalysts have been used as CE for conventional redox couple (I_3^-/I^-) in DSSCs. However, since large scale fabrication of DSSCs is impeded by high-cost and scarcity of Pt, alternative catalysts for IRR have been investigated intensively by researchers. Alternative catalysts are required to be not only inexpensive and Earth-abundant, but also highly active and conductive.

Various Pt-free materials received great attention as alternative CEs, such as transition metal alloys, transition metal compounds, and conducting polymers [32-52]. Another strong candidate is carbonaceous material. Carbon-based materials have high potential for CEs because of their low cost, high abundance and sufficient conductivity as well as high electrocatalytic activity and corrosion resistance for IRR [55]. However, since the intrinsic activity of carbonaceous materials is lower than that of Pt in iodide/triiodide electrolytes, carbon-based CEs can lower the overall cell efficiency compared with Pt CE.

In order to overcome this intrinsic limit of carbonaceous materials in real device, many researchers have attempted various strategies: (i) using materials with morphologies having high surface area to volume ratio, (ii) increasing active sites by making additional defect sites or (iii) doping heteroatoms. In case of the strategy (i), Kay and Grätzel, in 1996, introduced as a catalyst the mixture of graphite and carbon black for high conductivity and surface area respectively, and the cell showed an efficiency of 6.67% [32]. In 2006, Murakami et al. varied the thickness of the carbon black as the CE material and achieved efficiency of 9.1% with carbon black CE with thickness of 14.47 μm [56]. In addition to carbon black, carbon-based materials with high roughness factor, such as activated carbon [57],

mesoporous carbon [58-59], CNTs [60-61] and graphene [62-63], were applied as counter electrodes in DSSC.

In previous reports based on the strategy (ii), in order to overcome limited number of active sites for the I^-/I_3^- reduction in pure graphene, lattice surface defects and functional groups, such as oxygen or $-NHCO-$ were created [64-66]. In case of strategy (iii), heteroatoms, such as nitrogen (N), sulfur (S), boron (B), and phosphorous (P), were doped into the carbon lattice in order to improve the catalytic activity by breaking electroneutrality of carbon with slight decrease in conductivity [67-74]. Also, in case of nitrogen doping, it was confirmed that nitrogen states (including pyrrolic, pyridinic, quaternary N and N-oxide of pyridinic) affect the catalytic activity rather than the total N contents and among these N states, pyridinic N and quaternary N states can provide active sites for IRR [75]. It was also reported that co-doping of nitrogen and sulfur can have a synergistic effect on catalytic activity for IRR [76].

In contrast to synthetic materials, natural materials are not only abundant and cheap, but also do not require multistep preparation procedure. Natural materials like bamboo and oak wood [77], sea tangle [78], eggshell membrane [79], mangosteen peel waste [80], and pitch [81] were reported as carbonaceous CEs for DSSCs. However, since these natural materials mainly consist of almost pure carbon, they do not have any advantage in the

composition as an electrocatalyst for IRR. Also, some natural materials are too valuable to be just used as carbon precursors.

Coffee is one of the globe's largest agricultural commodities and about 7 billion kilograms of coffee is cultivated annually in over 70 countries [82]. However, most of used coffee-grounds are sent to landfill and even emit greenhouse gases while decomposing in landfill. Leftover coffee-grounds contains protein, caffeine, B vitamins, niacin, and riboflavin. Interestingly, these components are comprised of not only carbon, but also quite amount of nitrogen, which can provide active sites in case of carbon materials for electrochemical reactions [83-84].

The porous structure of material is a highly important characteristic in case of electrocatalysts due to its large specific surface area and ease of mass transport of electrolytes. Especially, microporous structure has strength due to its immense specific surface area that can provide large number of active sites for catalysts with low intrinsic activity like carbonaceous materials. Previous methods for preparing microporous carbonaceous materials are composed of carbonization process and following drying process, such as supercritical CO₂ drying process or freezing drying process, which is rigorous and time-consuming as well as expensive [85]. In contrast, chemical activation in the presence of ZnCl₂ salt is a fascinating method due to its simplicity and scalability in that carbonization and pore formation take

place simultaneously, which no longer requires additional drying process [86-87]. In addition, ZnCl_2 activation method have merits of producing robust microporous structure at low cost using nontoxic substances.

In this paper, we employed N, S co-doped carbon materials as a CE for triiodide reduction. The raw material of CE was obtained from leftover coffee-grounds. The carbonization and activation of coffee-grounds were proceeded in one-step process under Ar atmosphere by using ZnCl_2 salt. The activated coffee (AC) CE has the unique microporous structure, increasing surface area 10 times larger than that of non-activated coffee (NC) CE. DSSCs using AC-CE exhibits improved the fill factor (FF) and competitive overall cell efficiency compared with DSSCs using Pt CE.

Chapter 2. Experimental

2.1. Preparation of coffee counter electrodes

Activated coffee catalysts were prepared using the leftover coffee-grounds (Colombian SUPREMO, Costco) as the precursor and ZnCl_2 salt as a foaming agent. Coffee-grounds and ZnCl_2 salt were mixed in the ratio of 1:2 by weight and immersed in water to dissolve ZnCl_2 salt. After evaporating water from the mixture solution in vacuum oven at $80\text{ }^\circ\text{C}$ overnight, the uniform mixture of coffee-grounds and ZnCl_2 salt was obtained. Then, the mixture was transferred to a ceramic crucible and heat-treated to $800\text{ }^\circ\text{C}$ ($6.7\text{ }^\circ\text{C min}^{-1}$) and kept for 3 hours at this temperature in Ar atmosphere for carbonization and activation. After heat treatment, the mixture was immersed in 6 M HCl solution for overnight to remove any remaining ZnO, then washed several times with DI water and dried. For the preparation of non-activated coffee catalysts, the same coffee-grounds were carbonized at $800\text{ }^\circ\text{C}$ under Ar atmosphere without ZnCl_2 . The heating condition was the same as that of the activated one. The coffee counter electrodes were prepared by the spray method. For the preparation of coffee catalyst ink for spray, coffee catalysts were first grinded using a mortar and pestle and were dispersed in ethanol. Then, Nafion ionomer (5 wt%, Aldrich) with 5 wt% ratio was added to the solution and the solution was ultrasonicated for 30

min. The obtained catalyst ink was sprayed onto FTO glass and heat treated at 400 °C for 3 hr under Ar flow

2.2. Preparation of the Pt counter electrode and working electrode

The platinum counter electrodes were prepared by spin coating 300 μL Pt precursor solution of 50 mM H_2PtCl_6 in 2-propanol on FTO glasses (TEC-8, Pilkington) at 900 rpm. Then, Pt-coated counter electrodes were heated at 400 °C for 30 min in air to remove solvents and other impurities. For the preparation of the TiO_2 working electrodes, first TiO_2 blocking layer was coated onto the FTO glasses by immersing them in a 40 mM TiCl_4 aqueous solution at 70 °C for 30 min. After washing and drying, a colloidal TiO_2 paste (DSL 18NR-T, Dyesol Ltd.) was doctor bladed on the pretreated FTO glass and then, annealed at 500 °C for 30 min. After annealing process, these electrodes were dipped into a 16 mM TiCl_4 aqueous solution at 70 °C for 30 min and annealed at 450 °C for 30 min. The resulting TiO_2 electrodes were sensitized with *cis*-bis(isothiocyanato)bis(2,2'-bipyridyl-4,4-dicarboxylic acid) ruthenium (II) (N719 dye, Ohyoung Industrial Co.) by immersing them in a ethanol solution of 0.5 mM N719 dye at 30 °C for 24 hr.

2.3. Preparation of the iodide redox electrolytes

All chemicals mentioned below were purchased from Sigma-Aldrich and used without further purification. For the cyclic voltammetry (CV) measurements, Iodide and triiodide (I^-/I_3^-) redox electrolytes were prepared by mixing 10 mM LiI, 1 mM I_2 , and 0.1 M $LiClO_4$ in acetonitrile. For the symmetric dummy cell and solar cell analyses, iodide electrolytes were prepared by mixing 0.6 M 1-butyl-3-methylimidazolium iodide, 30 mM I_2 , 0.1 M guanidinium thiocyanate, and 0.5 M 4-*tert*-butylpyridine in a mixture of acetonitrile and valeronitrile (volumetric ratio = 85 : 15).

2.4. Fabrication of symmetric dummy cells and solar cells

For the fabrication of DSSC, the dye-sensitized working electrodes were assembled with the CEs using a thermoplastic sealant (Surlyn, Dupont) with 100 μ m thickness. The iodide electrolytes were injected into the assembled cell through a pre-drilled hole. Symmetric dummy cells for the evaluation of electrocatalytic activity of catalysts were fabricated with exactly the same method used for DSSC except that the two identical Pt, NC, or AC counter electrodes were assembled.

2.5. Material characterization, electrochemical analyses, and photovoltaic performance evaluation

Morphology of the coffee catalysts were characterized with a transmission electron microscope (TEM; Technai F20, 200kv). Morphology of the CE film on FTO glass were characterized with field emission scanning electron microscope (FE-SEM; ZEISS MERLIN Compact). N₂ adsorption/desorption isotherms were recorded on BELSORP-mini II, and Brunauer-Emmett-Teller (BET) analyses were used to obtain surface area. The pore size distribution was obtained by automatic gas and vapor adsorption analyzer (BEL Japan, Inc. BELSORP-max) using non-local density functional theory (NLDFT). Elemental analyses for C, N, and S were conducted by elemental analyzer (LECO Corp, US/CHNS-932). Energy Filtered-Transmission Electron Microscopy (EF-TEM) and Electron Energy Loss Spectroscopy (EELS; Jeol 2100F) analyses were conducted to obtain elemental distribution of the samples. An X-ray photoelectron spectroscopy (XPS; Thermo Fisher Scientific K-Alpha) analysis was conducted using a Al K α x-ray source (1486.6 eV). The carbon 1s peak served as internal reference, and the high resolution N1s spectra were used for the quantification of the different N sites. D/G ratio was analyzed using a Raman spectrometer (HORIBA LabRAM HV Evolution). Four point probe method was conducted using a sourcemeter (Keithley US/2400).

Cyclic voltammetry (CV) analysis and Tafel polarization plots were conducted by using a potentiostat (PGSTAT128N, Metrohm Autolab). CV analysis was measured with a three electrode system using a Pt mesh counter electrode and Ag/AgNO₃ reference electrode. CV curves were recorded in the potential range of -0.6 to 1.0 V at scan rates of 10 mV/s, 25 mV/s, 50 mV/s, 75 mV/s, and 100 mV/s. Tafel polarization plots were performed in a symmetric dummy cell and were recorded from -0.8 V to 0.8 V at a scan rate of 50 mV/s. Electrochemical impedance spectroscopy (EIS) was measured with symmetric dummy cells at temperature of 10°C, 20°C, 30°C, 40°C, and 50°C by using multichannel electrochemical workstation (ZIVE MP1). The EIS experiment was carried out in the frequency range of 50 mHz to 100 kHz with an AC amplitude of 10mV and an applied bias voltage of 0 V. The spectra results were fitted with Z-view software. Photovoltaic properties were characterized by solar simulators (XIL model 05A50KS source measure units, SERIC Ltd.) for DSSCs under a 1 sun condition (AM 1.5G with an incident light intensity of 100 mW/cm²), which was verified by a National Institute of Advanced Industrial Science and Technology (AIST, Japan) calibrated Si reference solar cell. The active area of the dye-sensitized TiO₂ film was 0.2025 cm². Prior to the photovoltaic measurement, a black aperture mask covered the devices in order to avoid overestimation of the conversion efficiency. The incident photon to current conversion efficiency (IPCE) of the

DSSCs was measured in the wavelength range of 300 nm to 800 nm with 10 nm wavelength width per each measurement point by using quantum efficiency measurement equipment (PV Measurements QEX10).

Chapter 3. Results and discussion

3.1. Material synthesis and characterization

Figure 3.1a shows the fabrication process of coffee counter electrodes. The inherently N-doped carbonaceous material was derived from natural resources as a Pt-free CEs for DSSCs. The material was made from leftover coffee-grounds that were produced after brewing the coffee. Since the intrinsic activity of carbonaceous materials for IRR reaction is lower than that of Pt, highly rough morphologies are critical for carbonaceous CEs to overcome this challenge. ZnCl_2 salt was added to the coffee grounds because ZnCl_2 salt serves as a foaming agent to achieve high surface to volume ratio of the catalysts [88]. The coffee-grounds without ZnCl_2 addition were carbonized under an Ar atmosphere at 800 °C. The obtained N-doped carbon materials are denoted as NC short for non-activated coffee. Whereas, in the presence of ZnCl_2 , coffee-grounds were carbonized and activated simultaneously. The obtained porous N-doped carbon materials are denoted as AC short for activated coffee. For the preparation of CEs, the catalyst ink made from NC and AC was sprayed onto FTO glass and dried at 400 °C for 3 h under Ar atmosphere. The 0.7 mg of each coffee catalyst was loaded on the 4 cm² area of the FTO glass. Figure 3.1b shows the schematic image of DSSCs using coffee catalysts as CE. Figure 3.2a-3.2d show the TEM images of coffee

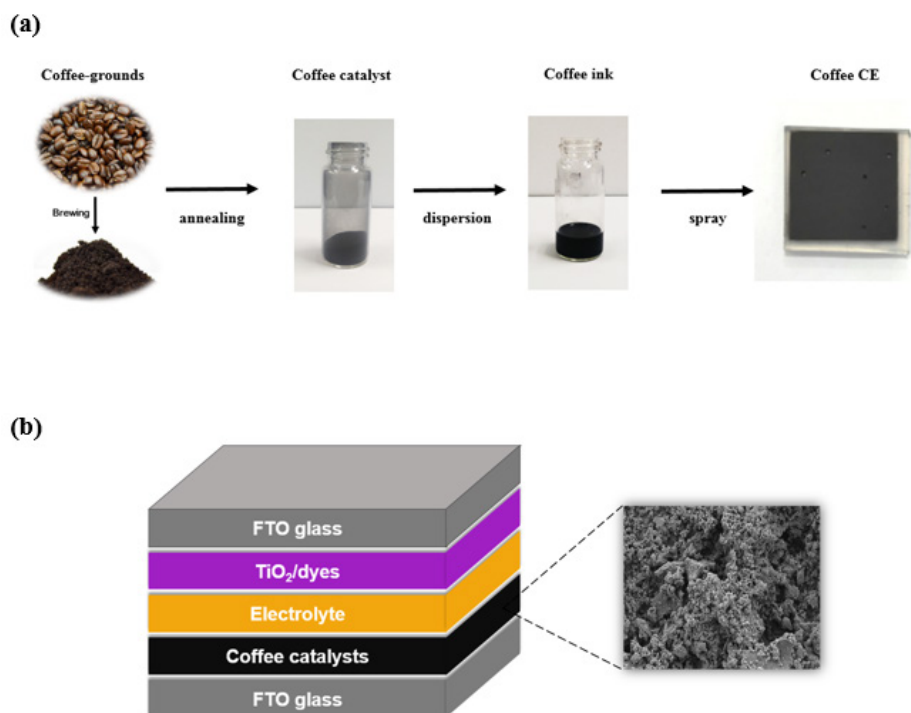


Figure 3.1. (a) Photographs showing the fabrication process of counter electrode using coffee catalysts. (b) Schematic of a dye-sensitized solar cell with coffee catalyst as counter electrode.

catalysts without (Figure 3.2a-3.2b) and with (Figure 3.2c-3.2d) the ZnCl_2 activation. The Figure 3.2a-3.2b show that NC is composed of a chunk of carbon. In contrast, Figure 3.1c-3.1d show that AC has foam-like morphology with highly porous structure. This porous structure was formed by ZnCl_2 sublimation and removing remaining ZnO which was made from ZnCl_2 .

Figure 3.3 shows the top-view SEM images of the coffee catalysts sprayed onto the FTO glass. In Figure 3.3a and 3.3b, top-view SEM images of NC counter electrode (CE) shows that NC-CE is constructed of micrometer-sized carbon chunks. Whereas, top-view SEM images of AC counter electrode (CE) in Figure 3.3c and 3.3d showed that AC catalysts formed nanostructure with rough surfaces. For further understanding of these structures, the cross-sectional morphologies of NC-CE and AC-CE were observed. The N_2 sorption isotherms of AC in Figure 3.4a showed typical type I/IV hybrid isotherms, indicating microporous and mesoporous structure was constructed through activation process. The BET surface area of AC is about 10 times as large as that of NC, while total pore volume of AC was nearly 20 times larger than that of NC (Table 3.1). The pore size distribution was obtained by applying nonlocal density functional theory (NLDFT) equilibrium model. Figure 3.4b confirmed that AC had both micropores and mesopores. Also, NC had micropores with diameters of about 1.1 nm that were assumed to occur

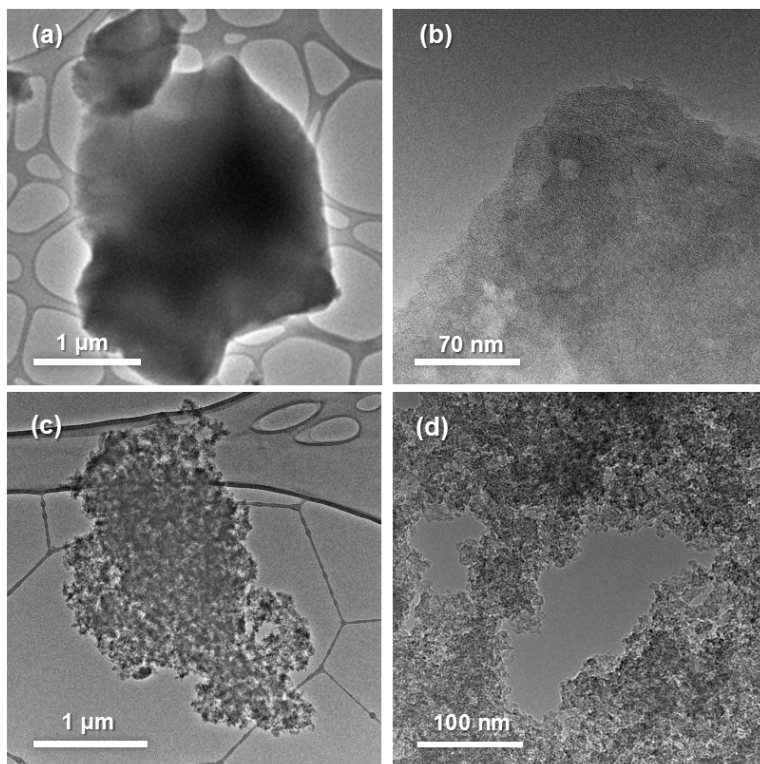


Figure 3.2. TEM image of coffee-grounds powder (a, b) after carbonization at 800 °C in Ar and (c, d) after carbonization and activation with ZnCl₂ simultaneously at 800 °C in Ar.

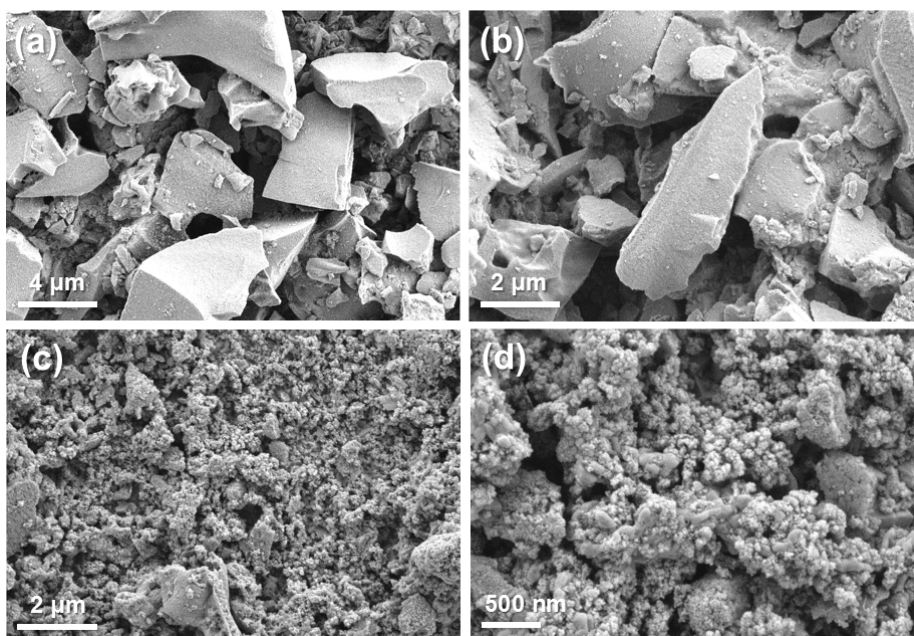


Figure 3.3. Top-view SEM images of coffee catalysts sprayed onto the FTO glass. (a, b) non-activated coffee catalyst, (c, d) activated coffee catalyst.

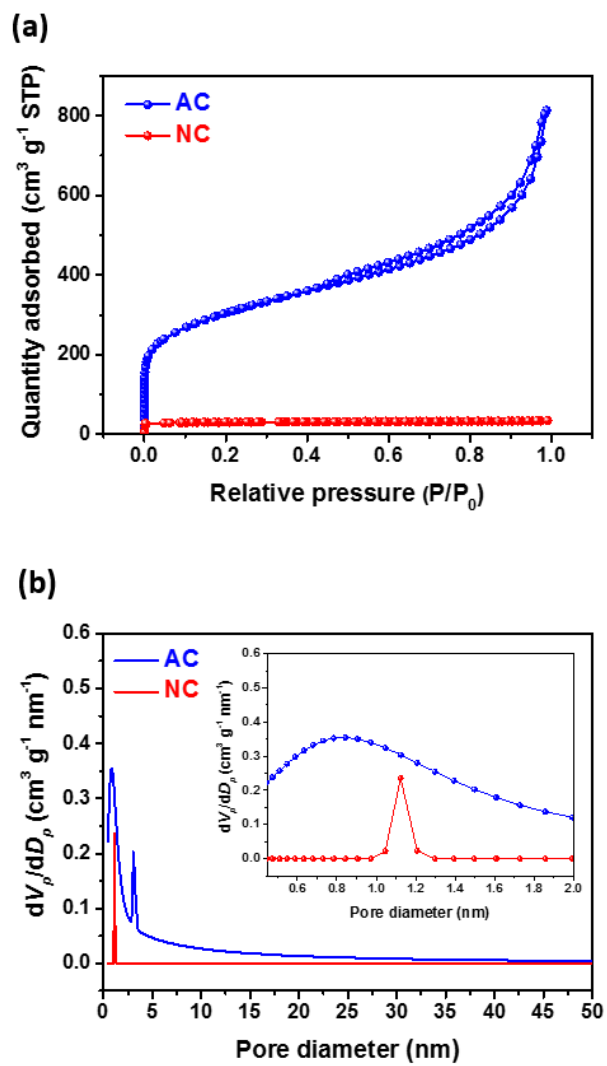


Figure 3.4. (a) Nitrogen adsorption and desorption isotherms. (b) Pore size distribution of coffee catalysts.

	BET surface area (m ² /g)	Total pore volume at p/p ₀ =0.99 (cm ³ /g)
NC	121.9	0.054
AC	1086.5	1.259

Table 3.1. Nitrogen sorption data of the NC and AC catalysts.

during annealing process at 800 °C. However, the amount of micropores in NC was so low that NC could not have high surface area. In Figure 3.5, X-ray diffraction (XRD) patterns of NC and AC sample displayed two broad diffuse bands centered around 2-theta position of 24°, and 43°, associated with diffraction from the [002] and [100] planes. The broad diffraction peaks implied that both N-doped carbons were constructed of an amorphous carbon structure after carbonization process. Also, AC showed broader and more diffuse peaks than NC, meaning more amorphous structure because a lump of carbon was shattered during activation process, which accorded with the SEM image in Figure 3.3.

Elemental analysis (EA) was conducted to identify compositions of NC and AC samples. The EA results were crosschecked using XPS survey spectra (Table 3.2a – 3.2b). The results showed that prepared coffee catalysts contain nitrogen and sulfur atoms. N/C ratio in NC catalyst was 1.3 and 1.74 respectively in EA and XPS, whereas, in case of AC catalyst, N/C ratio was 1.064 and 0.895 respectively in EA and XPS, which was slightly lower than that of NC catalyst. Also, in order to identify the doping sites of nitrogen and its content, high resolution N1s peak was investigated according to previous reports. By deconvoluting N1s spectra, four kinds of N states, including pyridinic N (398.5 eV), pyrrolic N (400.3 eV), graphitic N (401 eV) were distinguished depending on the bonding states of the N atom (Figure 3.6a).

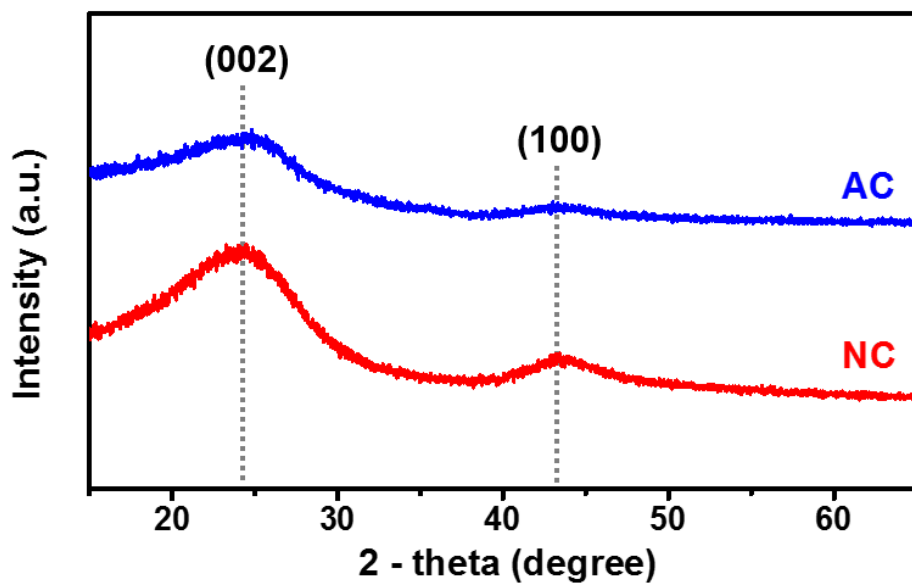


Figure 3.5. XRD patterns of NC and AC catalysts.

(a)

EA	C	N/C	S/C
NC	100	1.229	0.711
AC	100	1.064	0.896

(b)

XPS	N (%)	N/C	S/C
NC	1.58	1.739	0.110
AC	0.84	0.895	0.107

Table 3.2. Composition of NC and AC samples obtained from (a) EA, and (b) XPS.

It has been reported that pyridinic and graphitic N doping sites in nitrogen-doped carbonaceous materials provide active sites for IRR [35]. Compared to NC catalyst, the amount of pyridinic nitrogen and pyrrolic nitrogen decreased while that of graphitic nitrogen showed no big difference (Table 3.3 and Figure 3.6b). The decrease of total doping content is attributed to the reason that unstable dopant are peeled off with carbon during activation process. The fact that decrease of nitrogen content is originated from the decrease of pyridinic N and pyrrolic N, while concentration of graphitic N is similar, suggests that relatively unstable nitrogen functional groups located at edge sites are detached from the carbon lattice during ZnCl_2 activation process. In case of sulfur doping, atomic percent of sulfur of both samples are around 0.1 % and indicated no big difference of sulfur contents between NC and AC. Energy filtered transmission electron microscopy (EF-TEM) images in Figure 3.7 reveal that carbon, nitrogen, and sulfur are distributed over the entire structure, proving successful heteroatom doping.

To obtain insight into carbon structural changes, Raman spectra were acquired for NC and AC. As shown in Figure 3.8a, Raman spectra can be deconvoluted into four types of characteristic carbon resonance peaks around 1600 cm^{-1} , 1350 cm^{-1} , 1200 cm^{-1} and 1510 cm^{-1} . Peak around 1600 cm^{-1} (G band) corresponds to the stretching of the C-C bond in graphitic materials

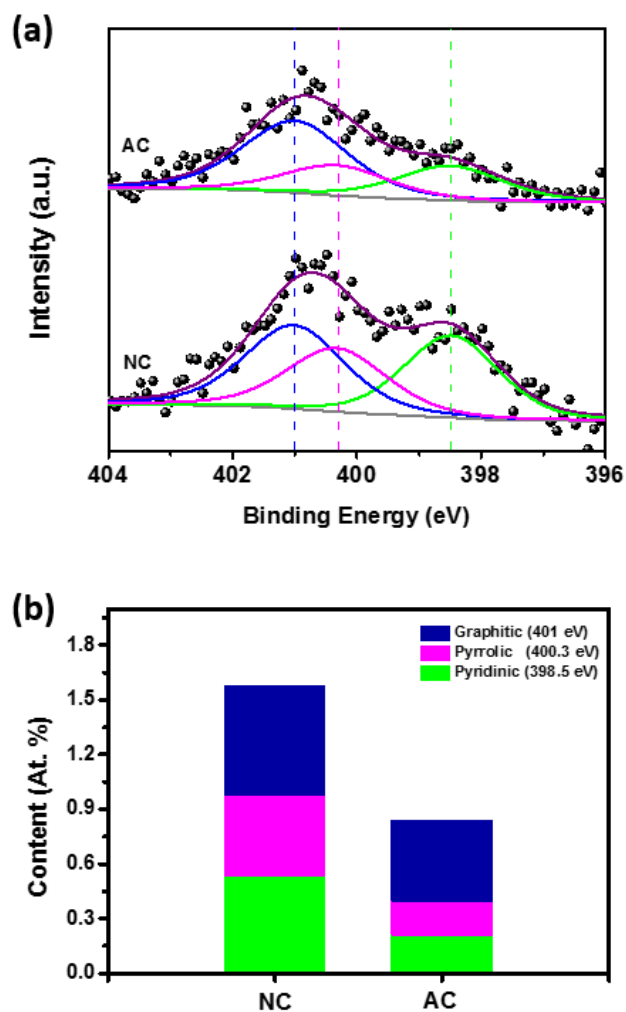


Figure 3.6. (a) High resolution N1s XPS spectra of coffee-grounds powder with and without ZnCl₂ activation. Deconvoluted nitrogen peaks: pyridinic-N (398.5 eV), pyrrolic-N (400.3 eV), graphitic-N (401 eV) (b) Content distributions of nitrogen states in NC and AC.

	Pyridinic	Pyrrolic	Graphitic
Relative amount (%)			
NC	33.2	47.8	15.4
AC	22.4	44.6	25.3
Absolute amount (At. %)			
NC	0.52	0.76	0.24
AC	0.19	0.37	0.21

Table 3.3. Content distributions of N states in NC and AC catalysts.

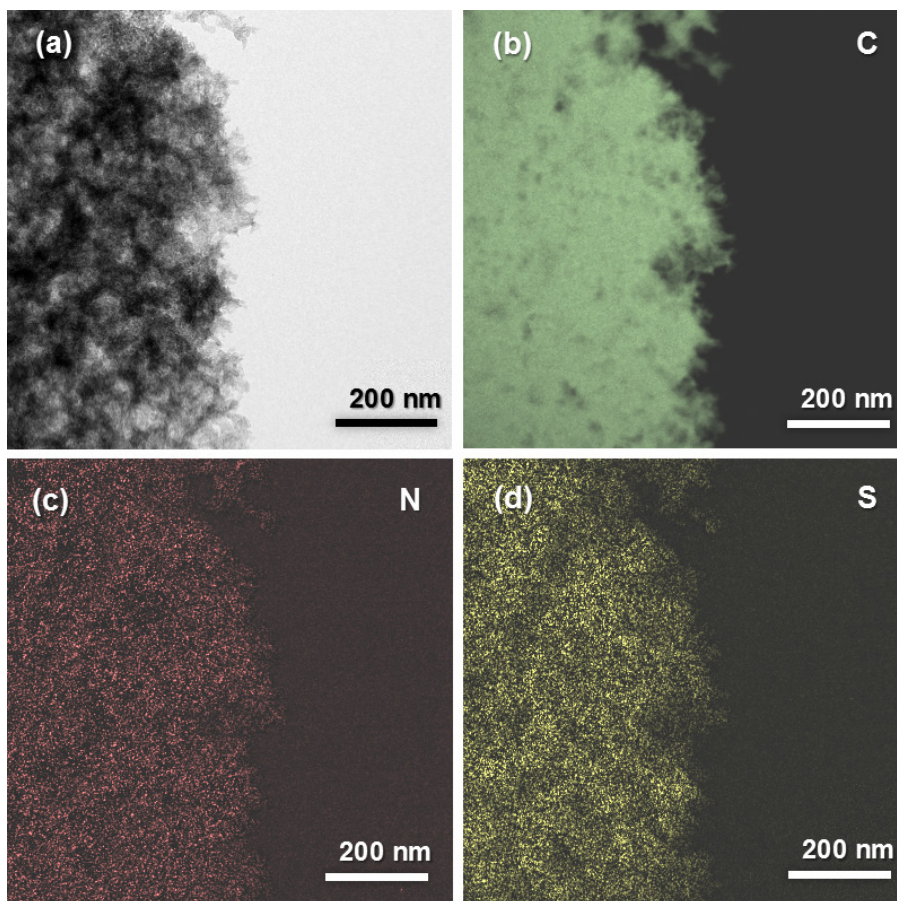


Figure 3.7. EF-TEM images of AC. (a) TEM image and the corresponding elemental mapping of (b) carbon, (c) nitrogen, (d) sulfur.

which is common to sp^2 -hybridized carbon atoms while peak around 1350 cm^{-1} (D band) means the presence of disorder in sp^2 -hybridized carbon from carbon atoms close to the edge sites. Additionally, two broad peaks around 1200 cm^{-1} and 1510 cm^{-1} are associated with aliphatic or amorphous structure and integrated five-member rings or heteroatoms in graphene-sheet structure, respectively [89]. Since defect sites in carbonaceous materials can provide the active sites for the catalytic reduction I_3^- to I^- and the D/G ratio provides an information about the overall order of carbon structure, each D/G ratio for NC and AC was calculated using peak area [65,90]. As shown in Figure 3.8b, D/G ratio of AC (2.41) was very slightly larger than that of NC (2.32), indicating no significant difference.

The electrical resistivity of NC and AC catalysts sprayed onto the glass substrates was measured using a four-point probe method (Table 3.4) The electrical resistivity and conductivity of NC catalyst film were $5.4 \times 10^{-3}\ \Omega \cdot m$ and 184.5 S/m , respectively. In case of AC catalyst film, the electrical resistivity and conductivity were $3.87 \times 10^{-2}\ \Omega \cdot m$ and 25.8 S/m , respectively. The lower conductivity of AC catalyst film compared to NC catalyst film was due to the smaller grain sizes and increased grain boundaries of AC catalysts, aggravating the connectivity between N-doped carbon catalysts.

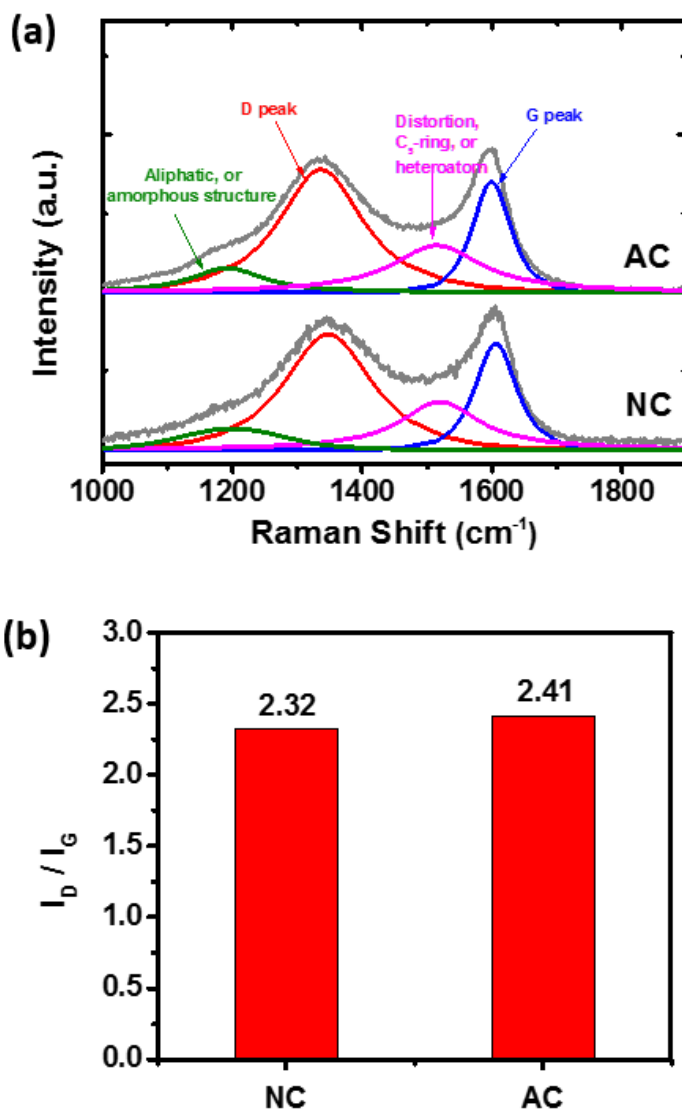


Figure 3.8. (a) Comparison of Raman spectra of NC and AC in the wavenumber range 1000 – 1900 cm⁻¹. (b) Comparison of D/G ratio in NC and AC.

	Four point probe		EIS
	ρ (Ω m)	σ (S/m)	R_s (Ω cm ²)
NC	5.4×10^{-3}	184.5	5.92
AC	3.87×10^{-2}	25.8	6.05

Table 3.4. Summary of electrical resistivity (ρ) and conductivity (σ) from a four-point probe and series resistance (R_s) from EIS of symmetrical cells.

3.2. Electrocatalytic activity and stability of the coffee electrodes

The electrocatalytic activity of the sprayed non-activated coffee, activated-coffee and platinized FTO electrodes were investigated by cyclic voltammetry (CV) analyses in I₂, LiI, and LiClO₄. As shown in Figure 3.9a, two clear pairs of redox peaks were observed in CV curves for each electrode. The more positive and negative pair of redox peaks correspond to the redox reaction (1) and (2), respectively.



Generally, the catalytic activity of a catalyst is related to the I⁻/I₃⁻ redox reaction. A higher cathodic peak current density (J_{pc}) and a smaller peak-to-peak voltage separation (E_{pp}) imply a higher catalytic activity [91]. The cathodic peak current densities were 2.057, 1.655, and 1.393 mA/cm² for AC, NC, and Pt electrodes. However, since non-faradaic current density largely contributed to peak current density for NC-CE and AC-CE, J_{pc} could not be used as an accurate activity descriptor. The peak-to-peak voltage separation (E_{pp}) for Pt electrode was 0.323 V which was smaller than 0.362 V and 0.471 V for NC and AC electrodes (Table 3.5). The smaller peak to peak separation of Pt electrode indicates that low overpotential is required for electrochemical reaction, which is consistent with more positive cathodic peak potential of Pt

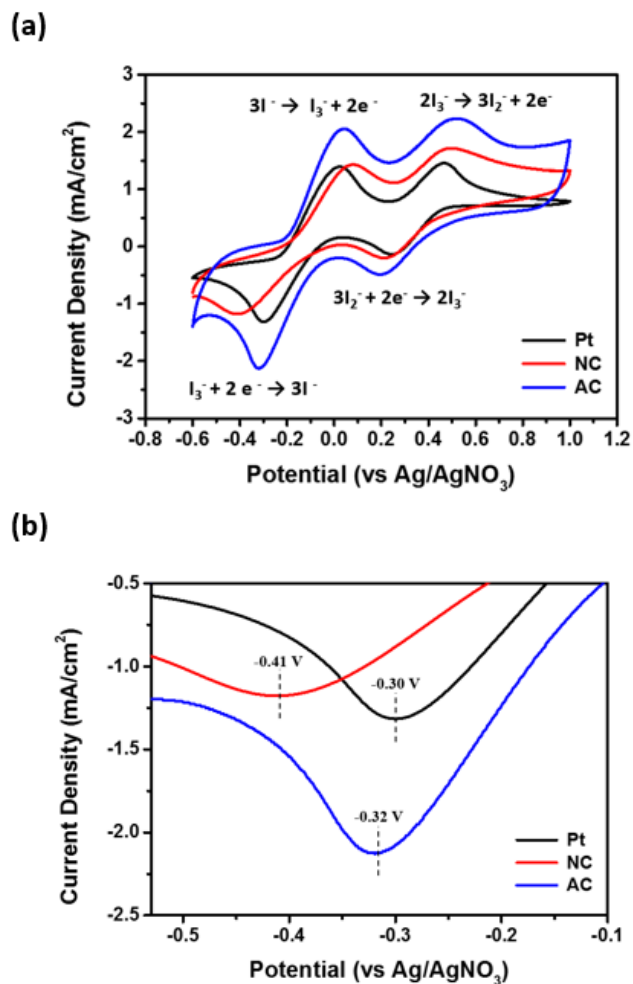


Figure 3.9. (a) Cyclic voltammograms obtained at a scan rate of 50 mV/s for oxidation and reduction of the I_3^-/I^- redox couple using different electrocatalysts as the WE, a Pt mesh as the CE, $Ag/AgNO_3$ as the reference electrode from -0.6 V to 1.0 V. (b) Cathodic peak potential of Pt, NC, and AC in I_3^-/I^- electrolytes.

	J_{pa} (mA/cm ²)	J_{pc} (mA/cm ²)	E_{anodic} (V)	$E_{cathodic}$ (V)	E_{pp} (V)
Pt	1.393	-1.32	0.023	-0.300	0.323
NC	1.655	-1.31	0.059	-0.412	0.471
AC	2.057	-2.13	0.043	-0.319	0.362

Table 3.5. Parameters obtained from cyclic voltammogram for the I_3^-/I^- redox reaction.

(-0.300 V) compared to that of AC (-0.319 V) and NC (-0.412 V) (Figure 3.9b). However, peak to peak voltage separation (E_{pp}) of porous electrode (in case of NC-CE and AC-CE) can be misinterpreted because contrary to the flat electrode, peak to peak separation of porous electrode can be altered not only by electrode kinetic parameters, but also by mass transport effect [92].

Also, the influence of potential scan rate on the peak currents of iodide was studied by CV at various scan rates (10, 25, 50, 75, 100 mV s^{-1}) for Pt, NC, and AC electrodes (Figure 3.10a-3.10c). Figure 3.10d depicts the linear correlation between peak current densities of I^-/I_3^- reduction and square roots of scan rates, indicating that charge transfer in the redox step is diffusion controlled [34]. The electrochemical stability of the Pt and coffee electrodes was investigated by using 100 consecutive CV cycles at a scan rate of 50 mV/s . As shown in Figure 3.11a-3.11c, shapes of CV curves were retained during CV cycles. In Figure 3.11d, no obvious attenuation of peak current densities for coffee electrodes as well as Pt electrode imply that coffee catalysts and Pt are quite stable for triiodide reduction reaction.

In order to investigate electrocatalytic activity of different catalysts, Tafel polarization analyses were conducted using symmetrical dummy cells at a scan rate of 50 mV/s at 20 °C. The Tafel polarization curves reveal a logarithmic current density (J) as a function of voltage (V). The superior electrocatalytic activity of the catalyst electrode can be inferred from higher

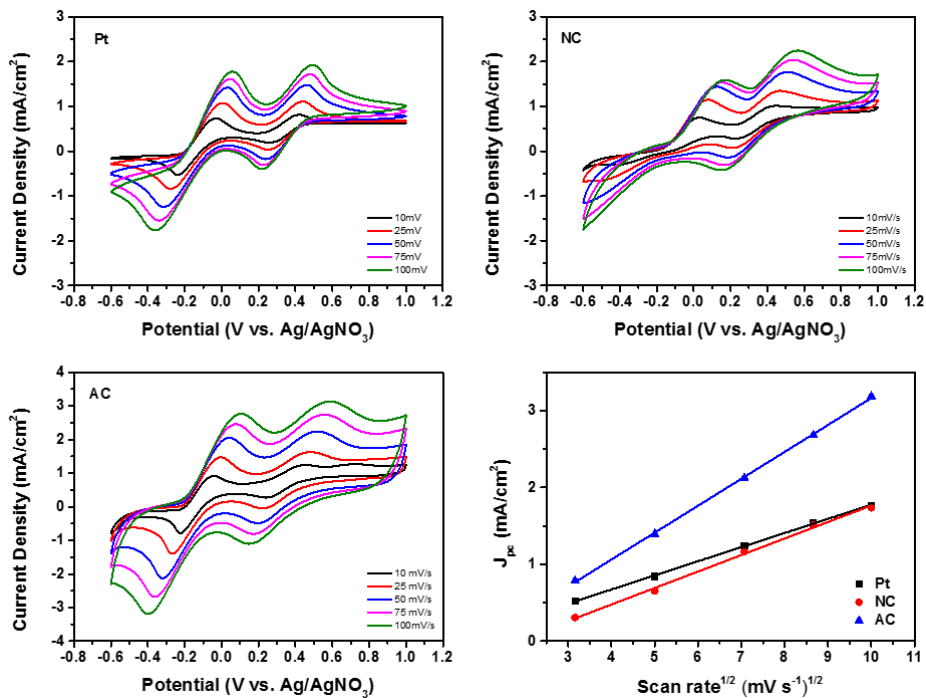


Figure 3.10. Cyclic voltammograms of (a) Pt, (b) NC, (c) AC CE for I₃⁻/I⁻ redox couples at different scan rates (from inner to outer: 10, 25, 50, 75, 100 mV/s). (d) Relationship between cathodic peak current density and square root of scan rates.

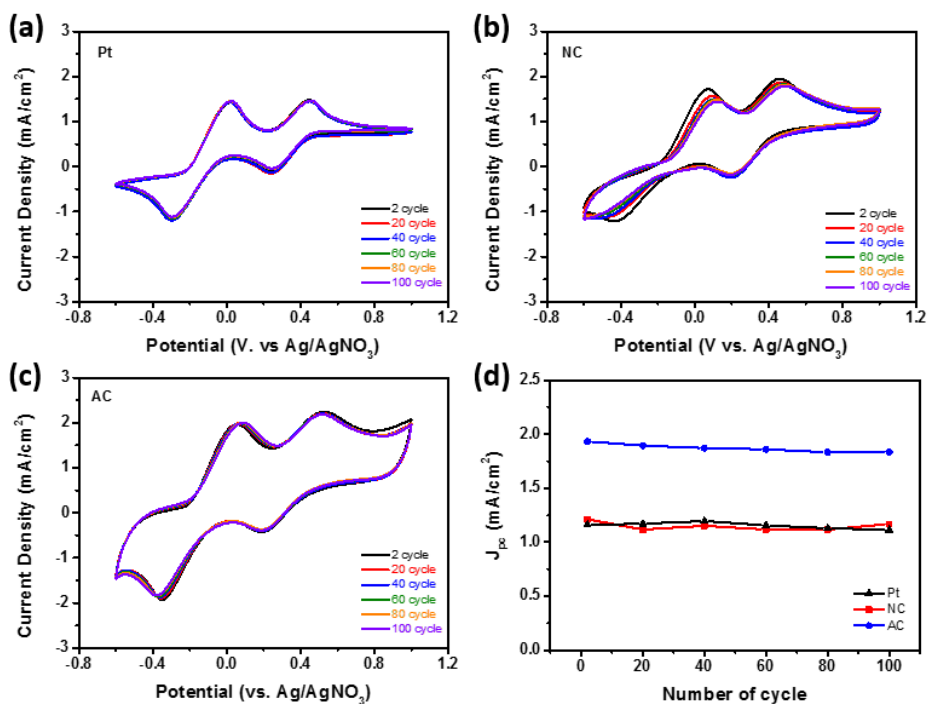


Figure 3.11. Cyclic voltammograms of 100 cycles using (a) Pt, (b) NC, (c) AC as working electrodes at a scan rate of 50 mV/s, (d) cathodic current density as a function of number of CV cycle.

exchange current density (J_0) and limiting diffusion current density (J_{lim}). A larger slope for anodic or cathodic branches implies higher exchange current density (J_0), while the intersection of cathodic branch with Y-axis in the Tafel plots corresponds to the limiting diffusion current density (J_{lim}). In Figure 3.12a, AC showed a higher exchange current density (J_0) having an order of $AC > Pt > NC$. However, diffusion limiting current density (J_{lim}) of three catalysts showed no obvious difference. These results suggest that the electrocatalytic activity of the AC is superior to the Pt and NC for the iodide redox couple. In order to obtain quantitative kinetic parameters for triiodide reduction reaction, electrochemical impedance spectroscopy (EIS) analyses were conducted using the same symmetrical dummy cells at open circuit condition (0 V applied across the dummy cell). Figure 3.12b shows the Nyquist plots obtained at 20 °C using Pt, AC, and NC electrodes. We used the equivalent circuit models shown in Figure 3.13a and 3.13b for Pt and coffee catalysts, respectively. Equivalent circuit model of Figure 3.13 comprises series resistance (R_s), charge transfer resistance (R_{ct}) at the electrolyte/electrode interface, constant phase element (CPE), and Warburg impedance (W_s). R_s is influenced by contact resistance between catalyst film and FTO glass, conductivity of the catalyst film, and solution resistance. R_{ct} and CPE are related to the electrocatalytic activity and the double layer capacitance (C_{dl}) respectively and determined from the first semicircle of

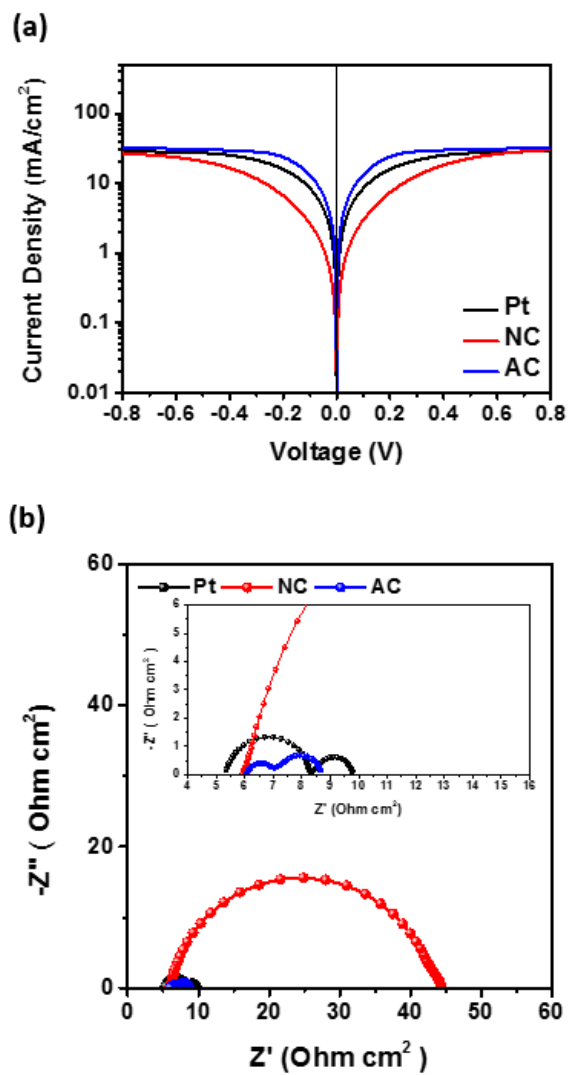


Figure 3.12. (a) Tafel polarization curves of symmetric dummy cells with Pt, NC, and AC counter electrodes for iodide electrolytes. (b) Impedance spectra of the symmetric dummy cells for iodide electrolytes, with the insets showing the enlarged spectra. Both analyses were conducted at 20 °C.

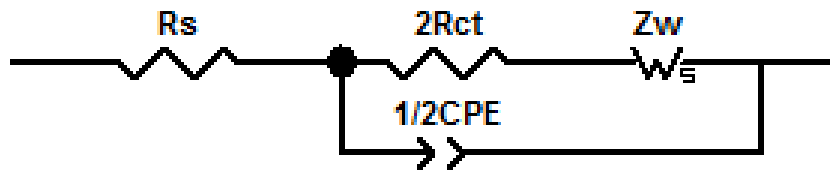


Figure 3.13. The equivalent circuit model for the impedance spectra of symmetric dummy cells shown in Figure 3.12b.

Nyquist plot. Whereas, W_s is related to the electrolyte diffusion and determined from the second semicircle of Nyquist plot. In Figure 3.12b, W_s showed no clear difference among three electrodes. R_s values of electrodes had an order of Pt ($5.33 \Omega \text{ cm}^2$) < NC ($5.92 \Omega \text{ cm}^2$) < AC ($6.05 \Omega \text{ cm}^2$). The higher R_s of AC electrode compared to NC electrode is in accordance with conductivities of electrodes (Table 3.4) measured by using four point probe method. As listed in Table 3.6, AC had a significantly lower R_{ct} value ($0.46 \Omega \text{ cm}^2$), followed by Pt ($1.46 \Omega \text{ cm}^2$) and NC ($18.69 \Omega \text{ cm}^2$). Exchange current density (J_0) value can also be calculated according to Equation (3),

$$J_0 = RT/nFR_{ct} \quad (3)$$

where R is the gas constant, T is the absolute temperature, n is the number of electrons which is two for I/I_3^- redox reaction, and F is the Faraday constant. J_0 had an order of NC (0.68 mA/cm^2) < Pt (8.64 mA/cm^2) < AC (27.62 mA/cm^2). These J_0 values indicating catalytic activity of the electrodes depend on both intrinsic catalytic activity and active area of the electrode.

However, since the double layer capacitance (C_{dl}) related to the surface roughness of the electrode had all different values, it was difficult to verify the origin of the catalytic activity of each electrode. Thus, in order to compare the intrinsic catalytic activity of the electrodes, activation energies for charge

	R_s ($\Omega \text{ cm}^2$)	R_{ct} ($\Omega \text{ cm}^2$)	C_{dl} ($\mu\text{F}/\text{cm}^2$)	J_0 (mA/cm^2)
Pt	5.33	1.46	36.5	8.64
NC	5.92	18.69	611.5	0.68
AC	6.05	0.46	5174.0	27.62

Table 3.6. Electrochemical parameters determined by fitting the impedance spectra of symmetrical dummy cells with Pt, NC, and AC electrodes.

transfer in I/I_3^- redox reaction were derived according to the Equation (4) (Arrhenius equation),

$$J_0 \propto k = A \exp(-E_a/RT) \quad (4)$$

where k is the rate constant, A is the pre-exponential factor related to the surface roughness, E_a is the apparent activation energy, R is the gas constant, T is the absolute temperature. EIS analyses were conducted at five different temperature conditions (283 K, 293 K, 303 K, 313 K, 323 K) as shown in Figure 3.14a. J_0 values were obtained from R_{ct} values using Equation (3) and activation energies for each electrode were obtained from slopes of linear plots ($\log J_0$ vs $1000/T$) as shown in Figure 3.14b. The obtained apparent activation energy in Table 3.7 had an order of Pt (28.34 kJ/mol) < NC (36.41 kJ/mol) < AC (38.16 kJ/mol). These results suggest that intrinsic catalytic activity was higher for Pt than N-doped carbon catalysts. Also notable is the fact that activation energy of NC was slightly higher than that of AC. According to previous reports [56, 94], active sites for catalysis in carbonaceous materials are located in the edge sites. The D/G ratios of NC and AC obtained from Raman spectra analyses in Figure 3.9b indicated that AC had slightly more defect sites than NC, but showed no significant difference. However, in XPS results of N-doping states (Table 3.3), absolute amount of pyridinic and graphitic N states, which can provide active sites for triiodide reduction reaction [35], was lower for AC compared to NC, because

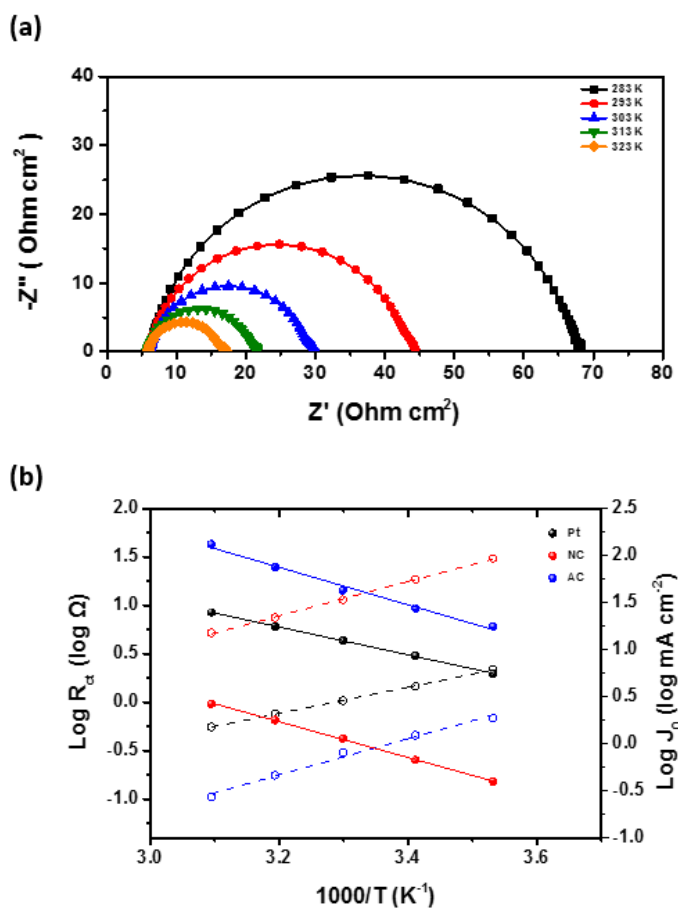


Figure 3.14. (a) Nyquist plots of symmetric dummy cell of NC electrode at five different temperature conditions. (b) Arrhenius plot of the temperature dependence of the charge transfer resistance (left ordinate) and exchange current density (right ordinate) to determine the apparent activation energy for triiodide reduction reaction with different counter electrodes.

	J_0 (mA/cm ²)					Slope (K)	E_a (kJ/mol)
	283 K	293 K	303 K	313 K	323 K		
Pt	5.56	8.64	12.53	17.73	25.00	-1.482	28.34
NC	0.40	0.68	1.14	1.80	2.67	-1.904	36.41
AC	17.75	27.62	42.92	76.25	132.60	-1.995	38.16

Table 3.7. Kinetic parameters for triiodide reduction reaction and obtained apparent activation energies on different counter electrodes.

of loss of N contents during activation process. The loss of pyridinic and graphitic N states of AC could give an explanation for the slightly increased apparent activation energy of AC electrode compared to NC electrode, though D/G ratio of AC was slightly higher than that of NC. To sum up, significantly larger J_0 value of AC compared to that of Pt and NC could be caused not by any intrinsic activity change, but by the increased effective surface area to volume ratio of the electrode by $ZnCl_2$ activation process.

3.3. Application of the coffee electrodes in dye-sensitized solar cells

For the device applications, Pt and coffee electrodes were directly used as counter electrodes in DSSCs. DSSCs were prepared by using N719 dye molecules with I_3^-/I^- electrolytes. The J - V curves measured under incident light of AM 1.5G condition (light intensity: 100 mW/cm^2) are shown in Figure 3.15a, and the photovoltaic parameters from J - V curves are tabulated in Table 3.8. The Pt-based reference DSSC exhibited a short circuit current density (J_{sc}) of 14.93 mA/cm^2 , an open circuit voltage (V_{oc}) of 0.760 V , a fill factor (FF) of 71.0% , and a power conversion efficiency (η) of 8.06% . Compared to Pt-based DSSC, the DSSC with AC-CE showed a slightly higher J_{sc} of 15.07 mA/cm^2 , a FF of 73.2% , and a η of 8.37% except a

similar V_{oc} of 0.759 V. Whereas, the DSSC with NC-CE showed a lower performance with J_{sc} of 12.70 mA/cm², a FF of 64.8 %, and a η of 6.25 % except a similar V_{oc} of 0.757 V. Among the parameters that determined the performance of DSSC, FF and J_{sc} showed clear difference for different CEs. FF is related to series resistance (R_s) and charge transfer resistance (R_{ct}), while J_{sc} is influenced by FF and total number of active sites of the CE [ref]. The slightly increased FF of AC-based DSSC compared to Pt-based DSSC matched well results from EIS analyses (Table 3.6), where sum of R_{ct} and R_s values was lower for AC than Pt. Also, a little increase in J_{sc} for AC-based DSSC can be explained by increase in FF . In the same way, lower FF of NC-based DSSC is attributed to the high charge transfer resistance. Meanwhile, much smaller J_{sc} value for DSSC using NC-CE compared to DSSC using Pt-CE or AC-CE was attributed to small FF and lower number of active sites. The lower number of active sites for NC-CE can be predicted from smaller C_{dl} value of NC electrode compared to that of AC electrode. However, in contrast to carbonaceous materials, there were a sufficient number of active sites for Pt even with much lower C_{dl} , because most exposed Pt surfaces are active sites for redox reaction. The IPCE spectra shown in Figure 3.15b were also consistent with the trend in J_{sc} values obtained from J - V curves.

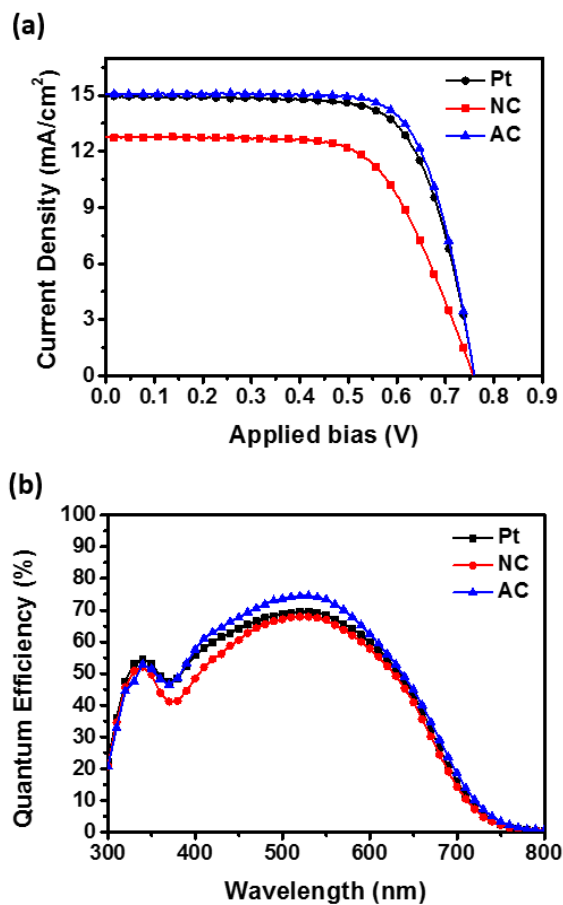


Figure 3.15. (a) Photocurrent density-voltage (J-V) curves of DSSCs with different counter electrodes under 1 sun illumination (AM 1.5 G, 100 mW/cm²). (b) IPCE spectra of the DSSCs with different counter electrodes.

	V_{oc} (V)	J_{sc} (mA/cm ²)	FF (%)	η (%)
Pt	0.760	14.93	71.0	8.06
NC	0.757	12.70	64.8	6.25
AC	0.759	15.07	73.2	8.37

Table 3.8. Summary of *J-V* characteristic for DSSCs using different counter electrodes under 1 sun illumination (AM 1.5 G, 100 mW/cm²)

Chapter 4. Conclusions

In this research, N,S co-doped carbon materials were made through the environmentally-friendly method that utilized waste coffee-grounds as heteroatoms-containing carbon precursors. The coffee electrode was fabricated by spraying the coffee-derived carbonaceous materials onto the FTO glass. The coffee electrode exhibited fine electrocatalytic activity for the redox reaction of iodide/triiodide redox couple, but still lower activity compared to the conventional Pt electrode. Therefore, the activated coffee (AC) electrode with highly porous structure was made by one-step carbonization and activation process of coffee-grounds using $ZnCl_2$ salt. The AC electrode was applied as the counter electrode for the dye-sensitized solar cells and showed superior performance to the conventional DSSC with Pt counter electrode. The higher electrocatalytic activity of the AC electrode was due to hierarchical porous structure that increased surface roughness of the electrode by 10 times. In dye-sensitized solar cells, high cost and scarcity of Pt have been the serious obstacle for the practical utilization and large-scale commercialization. In contrast, coffee-grounds are not only very cheap, abundant, and eco-friendly materials, but also the fabrication method of coffee electrode is simple, inexpensive and environmentally-friendly. Together with

the superior performance, these advantages of coffee-grounds are expected to facilitate the commercialization of the dye-sensitized solar cells.

Reference

- [1] Hagfeldt, A.; Boschloo, G.; Sun, L.; Kloo, L.; Pettersson, H. *Chem. Rev.* **2010**, *110*, 6595-6663.
- [2] O'Regan, B.; Grätzel, M. *Nature* **1991**, *353*, 737.
- [3] Nazeeruddin, M. K.; Kay, A.; Rodicio, I.; Humphry-Baker, R.; Mueller, E.; Liska, P.; Vlachopoulos, N.; Grätzel, M. *J. Am. Chem. Soc.* **1993**, *115*, 6382
- [4] Kuang, D.; Ito, S.; Wenger, B.; Klein, C.; Moser, J.-E.; Humphry-Baker, R.; Zakeeruddin, S. M.; Grätzel, M. *J. Am. Chem. Soc.* **2006**, *128*, 4146.
- [5] Haque, S. A.; Palomares, E.; Cho, B. M.; Green, A. N. M.; Hirata, N.; Klug, D. R.; Durrant, J. R. *J. Am. Chem. Soc.* **2005**, *127*, 3456
- [6] Haque, S. A.; Handa, S.; Peter, K.; Palomares, E.; Thelakkat, M.; Durrant, J. R. *Angew. Chem., Int. Ed.* **2005**, *44*, 5740
- [7] Bessho, T.; Zakeeruddin, S. M.; Yeh, C.-Y.; Diau, E. W.-G.; Grätzel, M. *Angew. Chem. Int. Ed.* **2010**, *49*, 6646.
- [8] Yella, A.; Lee, H.-W.; Taso, H. N.; Yi, C.; Chandiran, A. K.; Nazeeruddin, M. K.; Diau, E. W.-G.; Yeh, C.-Y.; Zakeeruddin, S. M.; Grätzel, M. *Science* **2011**, *334*, 629.
- [9] Lan, C.-M.; Wu, H.-P.; Pan, T.-Y.; Chang, C.-W.; Chao, W.-S.; Chen, C.-T.; Wang, C.-L.; Lin, C.-Y.; Diau, E. W.-G. *Energy Environ. Sci.* **2012**, *5*,

6460.

[10] Matthew, S.; Yella, A.; Gao, P.; Humphry-Baker, R.; Curchod, B. F. E.; Ashari- Astani, N.; Tavernelli, I.; Rothlisberger, U.; Nazeeruddin, M. K.; Grätzel, M. *Nat. Chem.* **2014**, *6*, 242.

[11] Feldt, S. M.; Gibson, E. A.; Gabrielsson, E.; Sun, L.; Boschloo, G.; Hagfeldt, A. *J. Am. Chem. Soc.* **2010**, *132*, 16714.

[12] Tsao, H. N.; Yi, C.; Moehl, T.; Yum, J.-H.; Zakeeruddin, S. M.; Nazeeruddin, M. K.; Grätzel, M. *ChemSusChem* **2011**, *4*, 591.

[13] Tsao, H. N.; Burschka, J.; Yi, C.; Kessler, F.; Nazeeruddin, M. K.; Grätzel, M. *Energy Environ. Sci.* **2011**, *4*, 4921.

[14] Grätzel, M. *Inorg. Chem.* **2005**, *44*, 6841.

[15] Ardo, S.; Meyer, G. J. *Chem. Soc. Rev.* **2009**, *38*, 115.

[16] Feng, X.; Shankar, K.; Varghese, O. K.; Paulose, M.; Latempa, T. J.; Grimes, C. A. *Nano Lett.* **2008**, *8*, 3781.

[17] Liu, B.; Aydil, E. S. *J. Am. Chem. Soc.* **2009**, *131*, 3985.

[18] Rensmo, H.; Keis, K.; Lindström, H.; Södergren, S., Solbrand, A.; Hagfeldt, A.; Lindquist, S.-E.; Wang, L. N.; Muhammed, M. *J. Phys. Chem. B* **1997**, *101*, 2598.

[19] Saito, M.; Fujihara, S. *Energy Environ. Sci.* **2008**, *1*, 280.

[20] Nguyen, H. M.; Mane, R. S.; Ganesh, T.; Han, S. H.; Kim, N. *J. Phys. Chem. C* **2009**, *113*, 9206.

- [21] Minoura, H.; Yoshida, T. *Electrochemistry* **2008**, *76*, 109.
- [22] Onwona-Agyeman, B.; Kaneko, S.; Kumara, A.; Okuya, M.; Murakami, K.; Konno, A.; Tennakone, K. *Jpn. J. Appl. Phys., Part 2* **2005**, *44*, L731.
- [23] Yamanaka, N.; Kawano, R.; Kubo, W.; Masaki, N.; Kitamura, T.; Wada, Y.; Watanabe, M.; Yanagida, S. *Chem. Commun.* **2005**, *6*, 740.
- [24] Nogueira, A.F.; Durrant, J.R.; Paoli, M.A. *Adv. Mater.* **2001**, *13*, 826.
- [25] Stergiopoulos, T.; Arabatzis, I.; Katsaros, G.; Falaras, P. *Nano Lett.* **2002**, *2*, 1259.
- [26] Wang, M.; Chamberland, N.; Breau, L.; Moser, J.; Humphry-Baker, R.; Marsan, B.; Zakeeruddin, S.; Grätzel, M. *Nat. Chem.* **2010**, *2*, 385.
- [27] Kato, F.; Hayashi, N.; Murakami, T.; Okumura, C.; Oyaizu, K.; Nishide, H. *Chem. Lett.* **2010**, *39*, 464.
- [28] Feldt, S.; Gibson, E.; Gabrielsson, E.; Sun, L.; Boschloo, G.; Hagfeldt, A. *J. Am. Chem. Soc.* **2010**, *132*, 16714.
- [29] Y. Liu, J. R. Jennings, Y. Huang, Q. Wang, S. M. Zakeeruddin and Grätzel, M. *J. Phys. Chem. C* **2011**, *115*, 18847.
- [30] Hardin, B.; Snaith, H.; McGehee, M. *Nat. Photonics* **2012**, *6*, 162.
- [31] Olsen, E.; Hagen, G.; Lindquist, S. *Sol. Energy Mater. Sol. Cells.* **2000**, *63*, 267.
- [32] Kay, A.; Grätzel, M. *Sol. Energy Mater. Sol. Cells.* **1996**, *44*, 99.
- [33] Wan, J.; Fang, G.; Yin, H.; Liu, X.; Liu, D.; Zhao, M.; Ke, W.; Tao, H.;

- Tang, Z. *Adv. Mater.* **2014**, *26*, 8101.
- [34] He, B.; Meng, X.; Tang, Q.; Li, P.; Yuan, S.; Yang, P. *J. Power Sources*, **2014**, *260*, 180.
- [35] Chang, P.; Cheng, K.; Chou, S.; Shyue, J.; Yang, Y.; Hung, C.; Lin, C.; Chen, H.; Chou, H.; Chou, P. *Chem. Mater.* **2016**, *28*, 2110.
- [36] Ahmad, S.; Deepa, M.; Singh, S. *Langmuir* **2007**, *23*, 11430.
- [37] Ha, Y. H.; Nokolov, N.; Pollack, S. K.; Mastrangelo, J.; Martin, B. D.; Shashidhar, R. *Adv. Funct. Mater.* **2004**, *14*, 615.
- [38] Biancardo, M.; West, K.; Frebs, F. C. *J. Photochem. Photobiol., A* **2007**, *187*, 395.
- [39] Xia, J.; Chen, L.; Yanagida, S. *J. Mater. Chem.* **2011**, *21*, 4644.
- [40] Wu, J.; Li, Q.; Fan, L.; Lan, Z.; Li, P.; Lin, J.; Hao, S. *J. Power Sources* **2008**, *181*, 172.
- [41] Jeon, S. S.; Kim, C.; Ko, J.; Im, S. S. *J. Mater. Chem.* **2011**, *21*, 8146.
- [42] Li, Z.; Ye, B.; Hu, X.; Ma, X.; Zhang, X.; Deng, Y. *Electrochem. Commun.* **2009**, *11*, 1768.
- [43] Li, Q.; Wu, J.; Tang, Q.; Lan, Z.; Li, P.; Lin, J.; Fan, L. *Electrochem. Commun.* **2008**, *10*, 1299.
- [44] Chen, X.; Tang, X.; He, B.; Lin, L.; Yu, L. *Angew. Chem. Int. Ed.* **2014**, *53*, 10799.
- [45] Kung, C. W.; Chen, H. W.; Lin, C. Y.; Huang, K. C.; Vittal, R.; Ho, K. C.

ACS Nano **2012**, *6*, 7016.

[46] Yang, Z.; Chen, C. Y.; Chang, H. T. *J. Power Sources* **2011**, *196*, 7874.

[47] Wu, M.; Lin, X.; Wang, Y.; Wang, L.; Guo, W.; Qi, D.; Peng, X.; Hagfeldt, A.; Grätzel, M.; Ma, T. *J. Am. Chem. Soc.* **2012**, *134*, 3419.

[48] Wu, M. X.; Lin, X.; Hagfeldt, A.; Ma, T. *Angew. Chem., Int. Ed.* **2011**, *50*, 3520.

[49] Wu, M. X.; Lin, X.; Hagfeldt, A.; Ma, T. *Chem. Commun.* **2011**, *47*, 4535.

[50] Jang, J.; Ham, D.; Ramasamy, E.; Lee, J.; Lee, J. S. *Chem. Commun.* **2010**, *46*, 8600.

[51] Gong, F.; Wang, H.; Xu, X.; Zhou, G.; Wang, J. S. *J. Am. Chem. Soc.* **2012**, *134*, 10953.

[52] Duan, Y.; Tang, Q.; Liu, J.; He, B.; Yu, L. *Angew. Chem. Int. Ed.* **2014**, *53*, 14569.

[53] Chen, X.; Hou, Y.; Zhang, B.; Yang, X. H.; Yang, H. G. *Chem. Commun.* **2013**, *49*, 5793.

[54] Hou, S.; Cai, X.; Wu, H.; Yu, X.; Peng, M.; Yan, K.; Zou, D. *Energy Environ. Sci.* **2013**, *6*, 3356.

[55] Wroblowa, H.S.; Saunders, A. *Electroanal. Chem. Interf. Electrochem.* **1973**, *42*, 329.

[56] Murakami, T. N.; Ito, S.; Wang, Q.; Nazeeruddin, Md. K.; Bessho, T.;

- Cesar, I.; Liska, P.; Humphry-Baker, R.; Comte, P.; Péchy, P.; Grätzel, M. *J. Electrochem. Soc.* **2006**, *153*, A2255.
- [57] Imotoa, K.; Takahashib, K.; Yamaguchib, T.; Komurab, T.; Nakamuraa, J.; Murata, K. *Sol. Energy Mater. Sol. Cells.* **2003**, *79*, 459.
- [58] Srinivasu, P.; Singh, S. P.; Islam, A.; Han, L. *Int. J. Photoenergy* **2011**, *2011*, 1.
- [59] Plonska-Brzezinska, M. E.; Lapinski, A.; Wilezewska, A. Z.; Dubis, A. T.; Villalta-Cerdas, A.; Winkler, K.; Echegoyen, L. *Carbon* **2011**, *49*, 5079.
- [60] Choi, H.; Kim, H.; Hwang, S.; Han, Y.; Jeon, M. *J. Mater. Chem.* **2011**, *21*, 7548.
- [61] Kaniyoor, A.; Ramaprabhu, S. *J. Appl. Phys.* **2011**, *109*, 124308.
- [62] Trancik, J. E.; Barton, S. C.; Hone, J. *Nano Lett.* **2008**, *8*, 982.
- [63] Noureldine, D.; Shoker, T.; Musameh, M.; Ghaddar, T. H. *J. Mater. Chem.* **2012**, *22*, 862.
- [64] Kavan, L.; Yum, J.; Grätzel, M. *ACS Nano* **2011**, *5*, 165.
- [65] Roy-Mayhew, J. D.; Bozym, D. J.; Punckt, C.; Aksay, I. A. *ACS Nano* **2010**, *4*, 6203.
- [66] Xu, C.; Li, J.; Wang, X.; Wang, J.; Wan, L.; Li, Y.; Zhang, M.; Shang, X.; Yang, Y. *Mater. Chem. Phys.* **2012**, *132*, 858.
- [67] Ju, M.J.; Jeon, I.Y.; Kim, J.C.; Lim, K.; Choi, H.J.; Jung, S.M.; Choi, I.T.; Eom, Y.K.; Kwon, Y.J.; Ko, J. *Adv. Mater.* **2014**, *26*, 3055.

- [68] Xue, Y.; Liu, J.; Chen, H.; Wang, R.; Li, D.; Qu, J.; Dai, L. *Angew. Chem. Int. Ed.* **2012**, *51*, 12124.
- [69] Zhai, P.; Wei, T.C.; Chang, Y.H.; Huang, Y.T.; Yeh, W.T.; Su, H.; Feng, S.P. *Small* **2014**, *10*, 3347.
- [70] Hou, S.; Cai, X.; Wu, H.; Yu, X.; Peng, M.; Yan, K.; Zou, D. *Energy Environ. Sci.* **2013**, *6*, 3356.
- [71] Fang, H.; Yu, C.; Ma, T.; Qiu, J. *Chem. Commun.* **2014**, *50*, 3328.
- [72] Jung, S.M.; Choi, I.T.; Lim, K.; Ko, J.; Kim, J.C.; Lee, J.J.; Ju, M.J.; Kim, H.K.; Baek, J.B. *Chem. Mater.* **2014**, *26*, 3586.
- [73] Wang, Z.; Li, P.; Chen, Y.; He, J.; Liu, J.; Zhang, W.; Li, Y. *J. Power Sources* **2014**, *263*, 246.
- [74] Yang, W.; Ma, X.; Xu, X.; Li, Y.; Raj, S.; Ning, G.; Wang, A.; Chen, S. *J. Power Sources* **2015**, *282*, 228.
- [75] Hou, S.; Cai, X.; Wu, H.; Yu, X.; Peng, M.; Yan, K.; Zou, D. *Energy Environ. Sci.* **2013**, *6*, 3356.
- [76] Chen, J.; Mao, Y.; Wang, H.; Hu, P. *ACS Catal.* **2016**, *6*, 6804.
- [77] Jiang, Q.W.; Li, G.R.; Wang, F.; Gao, X.P. *Electrochem. Commun.* **2010**, *12*, 924.
- [78] Wang, L.; Shi, Y.; Bai, X.; Xing, Y.; Zhang, H.; Wang, L.; Guo, W.; Wang, N.; Ma, T.; Grätzel, M. *Energy Environ. Sci.* **2014**, *7*, 343.
- [79] Wang, C.; Liao, J.; Chung, S.; Manthiram, A. *Adv. Energy Mater.* **2015**,

5, 1401524.

[80] Maiaugree, W.; Lowpa, S.; Towannang, M.; Rutphonsan, P.; Tangtrakarn, A.; Pimanpang, S.; Maiaugree, P.; Ratchapolthavisin, N.; Sangaroon, W.; Jarernboon, W.; Amornkitbamrung, V.; *Sci. Rep.* **2015**, *5*, 15230.

[81] Yang, W.; Ma, X.; Xu, X.; Li, Y.; Infant Raj, S.; Ning, G.; Wang, A.; Chen, S. *J. Power Sources* **2015**, *282*, 228.

[82] Zuorro, A.; Lavecchia, R. *J. Cleaner Prod.* **2012**, *34*, 49.

[84] Guo, D.; Shibuya, R.; Akiba, C.; Saji, S.; Kondo, T.; Nakamura, J. *Science* **2016**, *351*, 6271.

[85] Long, Y.; Zhang, C. C.; Wang, X. X.; Gao, J. P.; Wang, W.; Liu, Y. *J. Mater. Chem.* **2011**, *21*, 13934.

[86] Pampel, J.; Fellinger, T. *Adv. Energy Mater.* **2016**, *6*, 1502389.

[87] Yu, Z.; Li, G.; Fechler, N.; Yang, N.; Ma, Z.; Wang, X.; Antonietti, M.; Yu, S. *Angew. Chem. Int. Ed.* **2016**, *55*, 1.

[88] Yue, Z.; Mangun, C. L. *J. Economy, Carbon* **2002**, *40*, 1181.

[89] Wu, G.; Johnston, C.M.; Mack, N.H.; Artyushkova, K.; Ferrandon, M.; Nelson, M.; Lezama-Pacheco, J. S.; Conradson, S.D.; More, K.L.; Myersd, D.J.; Zelenay, P. *J. Mater. Chem.* **2011**, *21*, 11392.

[90] Wang, H.; Sun, K.; Tao, F.; Stacchiola, D.J.; Hu, Y. H. *Angew. Chem. Int. Ed.* **2013**, *52*, 9210.

[91] Yang, Z.; Li, L.; Luo, Y.; He, R.; Qiu, L.; Lin, H.; Peng, H. *J.*

Mater.Chem. A **2013**, *1*, 954.

[92] Menshykau, D.; Compton, R. G. *Electroanalysis* **2008**, *22*, 2387.

[93] Ju, M.J.; Jeon, I.; Kim, H.M.; Choi, J.I.; Jung, S.; Seo, J.; Choi, I. T.; Kang, S.H.; Kim, H.S.; Noh, M. J.; Lee, J.; Jeong, H.Y.; Kim, H.K.; Kim, Y.; Baek, J. *Sci. Adv.* **2016**, *56*, 1501459.

[94] Veerappan, G.; Bojan, K.; Rhee, S. *ACS Appl. Mater. Interfaces* **2011**, *3*, 857.

국문초록

전세계적으로 에너지 고갈 및 환경파괴 문제가 심화됨에 따라 화석연료의 대안으로서 신 재생에너지가 점점 중요해지고 있다. 여러 신 재생에너지원들 중에, 염료감응태양전지는 제조과정이 간단하고, 가격이 저렴하면서도 높은 에너지전환 효율을 갖기 때문에 크게 주목 받고 있다. 그러나 일반적으로 트리오오드화물의 환원 반응에 사용되어 오던 백금 촉매는 가격이 비싸고 매장량이 적다는 한계점을 지니기 때문에, 염료감응태양전지의 대량생산을 위해서는 좀 더 저렴한 가격의 대체촉매가 필요한 실정이다. 대체 전기화학촉매는 가격이 저렴하면서도 풍부할 뿐만 아니라 전도성이 있고 전기화학촉매로서의 높은 활성을 가져야 한다.

이러한 조건을 만족시키는 대체 촉매로서 백금 기반의 합금물질, 전이금속 기반의 합금물질, 전도성 고분자, 그리고 탄소 계 물질 등이 연구되어 왔다. 이러한 물질들 중, 탄소 계 물질은 풍부하면서도 가격이 훨씬 저렴하다는 이점을 갖는 반면, 트리오오드화물의 환원 반응에 대해 낮은 촉매활성을 갖는다는 한계점도 갖고 있다. 탄소 계 물질의 낮은 촉매활성을 극복하기 위해서, 전극의 형태를 바꾸어 표면적을 증가시키거나, 이종원자를 도핑하여 활성 사이트의 수를 증가시키는 등의 방법들이 연구되어 왔다. 그러나 이러한 방법들은 비싼 장비를 필요로 한다거나, 유해한 환경 또는 복

잡한 조건에서만 적용 가능하다는 한계점들을 갖는다.

이번 연구에서는 커피 찌꺼기를 친환경적인 전기화학촉매, 특히 트리오오드화물의 환원 반응에 대한 전기화학촉매로 사용하였다. 커피 찌꺼기는 이중원자를 포함하고 있는 탄소 전구체로서 사용하였고, 염화아연 염을 이용한 단일 공정으로 커피찌꺼기를 탄소화 및 활성화시켰다. 이렇게 얻어진 커피촉매의 잉크를 FTO 유리 기판 위에 스프레이하는 방식으로 상대전극을 제작하였다. 활성화된 커피 전극은 비활성화 된 커피 전극에 비해 본질적인 촉매 활성은 거의 감소하지 않은 반면, 전극 표면 면적은 10배 가량 증가하였다. 이로 인해 활성화 된 커피로 만든 상대전극과 백금 상대전극의 전하전달저항 값은 각각 $0.46 \Omega \text{ cm}^2$ 과 $1.46 \Omega \text{ cm}^2$ 으로, 활성화 된 커피 상대전극이 백금 상대전극 보다 우수한 전기화학적 촉매활성을 보였다. 또한 활성화 된 커피 상대전극을 염료감응태양전지에 적용했을 때, 태양전지는 73.2 % 의 필팩터, 15.07 mA/cm^2 의 단락 전류, 그리고 8.37%의 에너지 전환 효율을 보였다. 반면, 백금 상대전극을 사용한 염료감응태양전지는 71.0 % 의 필팩터, 14.93 mA/cm^2 의 단락 전류, 그리고 8.06 %의 에너지 전환 효율 값을 가지며, 활성화 커피 전극에 비해 낮은 성능을 보였다.

이번 연구에서는 저렴하면서도 풍부한 커피 찌꺼기를 이용하여 전기화학 촉매를 만들었고, 이를 염료감응 태양전지의 상대전극으로 사용할 시 기존의 값 비싼 백금 물질을 성공적으로 대체 할

수 있다는 것을 입증하였다.

핵심어 : 염료감응태양전지, 상대전극, 트리오오드화물 환원반응,
커피 찌꺼기, 염화아연 염을 이용한 활성화

학 번 : 2015-21024

성명 : 손 윤 준